Investigating helium-layer stripping in the interacting SN 2021efd

Master's Thesis
University of Turku
Dept. of Physics and Astronomy
Astronomy
June 2024
BSc Niko Pyykkinen
Supervised by:
Docent Hanindyo Kuncarayakti
Dr. Takashi Nagao
Prof. Seppo Mattila

University of Turku
Department of Physics and Astronomy

Pyykkinen, Niko: Constraints on the helium layer stripping mechanism in stripped-envelope supernova 2021efd

Master's thesis, 46 p.
Astronomy
June 2024

Some stars meet their ends in supernovae (SN) explosions. Massive stars ($\gtrsim 8$ $M_\odot$) at the end of their stellar evolution suffer a core-collapse and explode as core-collapse supernovae (CCSNe). SNe have diverse observational properties and are divided into classes based on them. Much can be known about the star that exploded from the SN it produced.

Stripped-envelope supernovae (SESNe) are explosions of massive stars that lost a part of the hydrogen envelope (Type IIb), the whole hydrogen envelope (Type Ib), or the hydrogen envelope and the helium layer (Type Ic). Evidence has accumulated to support a binary interaction as the stripping mechanism for the hydrogen envelope. The mechanism responsible for the helium-layer stripping for the progenitors of Type Ic SNe is still an open question.

In this thesis, I performed an in-depth analysis of the spectroscopic and photometric data of the peculiar Type Ib SN 2021efd. The light curve of SN 2021efd has an excess at late phases compared to the level that is expected from the decay of ^{56}Ni. I analyzed the spectra of SN 2021efd and concluded that the excess luminosity was caused by interaction of the ejecta with hydrogen-poor circumstellar material. I derived the ejecta parameters and the progenitor star mass and concluded that they do not separate SN 2021efd from the general population of SESNe. I estimated the mass-loss rate of the progenitor star by comparing the interaction luminosity in SN 2021efd to numerical calculations. Based on the high mass-loss rate, I concluded that the mass-loss mechanism is not consistent with line-driven wind. Instead, I suggest that the mass loss could have happened in eruptions.

Keywords: Supernovae, supernova progenitors, core-collapse supernovae, stripped-envelope supernovae, interacting supernovae, SN 2021efd, mass-loss mechanism, helium stripping, light curve model

Contents

1 Introduction

Supernovae are terminal explosions of stars. These events are among the brightest in the universe and they can momentarily outshine their host galaxies. SNe greatly impact the evolution of galaxies as they increase the *metallicity* of the galaxies which in turn affects star formation. Metallicity is the abundance of elements heavier than helium. Terminal explosions of massive stars ($\gtrsim$ 8 $M_\odot$) are called *core-collapse supernovae* (CCSNe). Factors such as metallicity, initial mass, and possible binary evolution determine the properties of the eventual explosion of the star. Thus from CCSNe we can learn much about the final states of massive stars. Not all SNe come from massive stars. When a low-mass star reaches the end of its life, it sheds its outer layers and becomes a white dwarf star. Upon accreting mass beyond a stable limit a runaway nuclear reaction will cause a white dwarf to explode as a *thermonuclear supernova*.

1.1 Classification of supernovae

The classification scheme of SNe focuses primarily on spectral features, although other qualities such as brightness and light curve shape are also used in order to differentiate between several subtypes. The schematic diagram of the classification scheme is displayed in figure 1.

The first quality that is usually looked for is the presence of hydrogen in the spectra. SNe with hydrogen in their spectra are classified as Type II SNe and ones without as Type I SNe. Type I SNe are further divided into subtypes of Ia, Ib, and Ic. Types Ib and Ic are sometimes collectively called Type Ib/c. Type Ia SNe have a stronger Si II absorption line at 6150 Å than Type Ib/c SNe. Type Ia SNe are thermonuclear SNe caused by explosions of white dwarfs. Type Ib SNe have helium lines in their spectra which are not present in Type Ic SNe. The most prominent line is the He I line at 5876 Å. Type Ic SNe have weaker Si II absorption lines than

Ia and do not have helium lines.[1]

All Type II SNe subtypes can not be distinguished by spectra alone. These spectroscopically regular Type II SNe typically have a phase when the magnitude is either linearly decaying or remains constant for ~ 100 days. These two subtypes are called Type IIL and Type IIP respectively. Other Type II SNe can be identified based on their spectral features. These are Type IIn SNe, which have narrow lines caused by the collision of the ejected material with *circumstellar material* (CSM) (see chapter 1.5) and Type IIb SNe, which have hydrogen in their spectra at early phases but later evolve to be spectroscopically similar to Type Ib SNe. [1]

There are further a few SN subtypes worth mentioning. Type Ibn SNe have largely the same lines present as Type Ib SNe but like Type IIn SNe, they have narrow lines in their spectra. Type Ic-BL are Type Ic SNe with very broad lines due to high ejecta velocity. [1]

There are also so-called *superluminous supernovae* which are divided into SLSN I and SLSN II depending on whether hydrogen is present. Most SLSN II are possibly explained as brighter end of Type IIn SN population [2]. They have no clear threshold magnitude but some reach magnitudes $\lesssim -20$ mag. Spectroscopically SLSN I have similarities with Type Ic SNe but are more luminous and have additional unexplained features. A threshold magnitude of $\lesssim -19.8$ mag has been suggested. [3]

1.2 Explosion mechanism of core-collapse supernovae

All SNe mentioned in chapter 1.1 excluding Type Ia are *core-collapse supernovae* (CCSNe). Stars fuse atoms in their cores, which is what produces the energy stars release. Initially, the material at the core is mostly hydrogen, which fuses into helium. After hydrogen is exhausted, sufficiently massive stars will fuse helium into carbon and carbon again into heavier elements. When a star with an initial mass

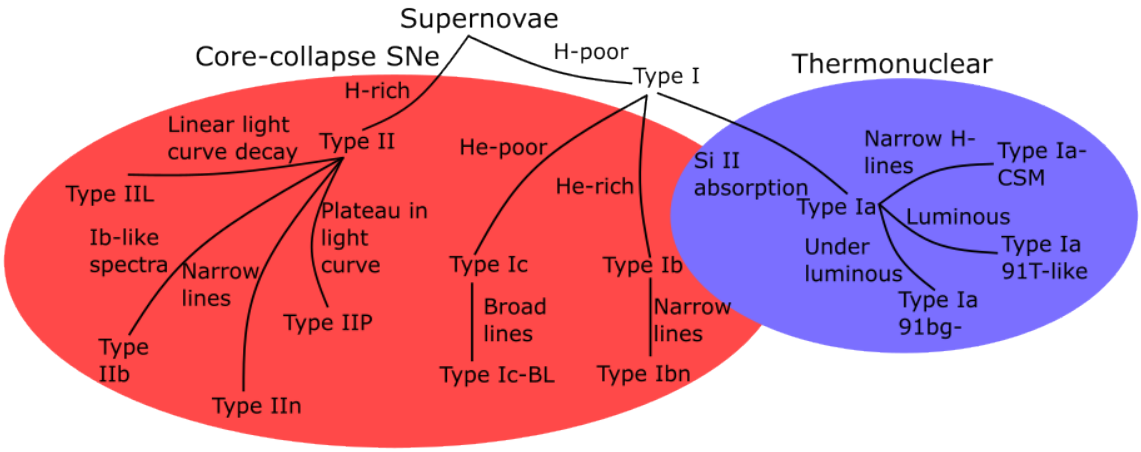

Figure 1. Figure illustrating the classification scheme of SNe. Some rare subtypes are not included. Core-collapse supernovae are on the left within the red background and thermonuclear SNe are on the right within the blue background.

greater than $\sim$8 $M_\odot$ reaches the end of its stellar evolution, it has a core of iron. Iron is the most stable element. Therefore it does not release energy when it fuses to form heavier elements.

The iron in the core of the star can go through two kinds of reactions: *electron capture* reactions and *photodisintegration*. In the electron capture reactions, a proton in the nucleus of an iron atom absorbs an electron, turning the proton into a neutron and releasing a neutrino,

$$p + e^- \rightarrow n + \nu_e,$$

where p is the proton, $e^-$is the electron, n is the neutron and ν_e is the neutrino. Electron degeneracy pressure prevents the core from collapsing. Electron pressure decreases when they are captured by the iron nuclei.

Photodisintegration means that the nucleus of an atom, in this case, the iron nucleus absorbs a high-energy photon and splits into helium nuclei which split into neutrons and protons,

$$^{56}\mathrm{Fe} + \gamma \rightarrow 13\ ^4\mathrm{He} + 4n$$

$$^4\mathrm{He} + \gamma \rightarrow 2p + 2n,$$

where γ is the high-energy photon.

Regardless of whether photodisintegration or electron capture is dominant, the iron core is only capable of undergoing endoergic reactions. These reactions take energy away from the electron or radiation pressure, which support the structure of the star, thus causing the core to collapse.

Due to the increased pressure in the core, increased amounts of electron capture reactions occur. This in turn increases the neutron density of the core. The collapse of the core stops when matter at the center becomes so dense that the neutron degeneracy pressure becomes dominant over gravity. This critical density is called *nuclear density*. Now a proto-neutron star has formed. The outer layers will then bounce on the surface of this proto-neutron star forming an outward-propagating shock wave.

Most of the energy released in the core collapse (~ 99 %) is released in the form of neutrinos created in the electron capture reactions. All but ~ 1 % of these neutrinos escape the star but the neutrinos that interact with matter heat the material in the shock. These effects combined are enough to propel the material to space. [4][5]

1.3 Post-explosion evolution of core-collapse supernovae

In the ejected material, the heating of the inner layers by the shock causes explosive nucleosynthesis to take place. This energy input makes even endoergic nuclear reactions possible, i.e., nucleosynthesis to heavier elements than iron. The proto-neutron star at the center eventually becomes either a neutron star or a black hole. If the amount of falling-back material is enough for the gravity of the neutron star to overcome the neutron degeneracy pressure, the outcome will be a black hole.

Due to the explosive nucleosynthesis, the ejected material contains some $\sim 10^{-1}$ $M_\odot$ of Nickel-56. This is a radioactive isotope with a half-life of 6 days and decays to radioactive Cobalt-56, which has a half-life of 77 days, and decays to stable

Iron-56.

$$^{56}\mathrm{Ni} + e^- \rightarrow ^{56}\mathrm{Co} + \gamma + \nu_e$$

$$^{56}\mathrm{Co} + e^- \rightarrow ^{56}\mathrm{Fe} + \gamma + \nu_e$$

The energy released by the radioactive decay acts as a source of radiation for SNe. Radioactive decay is not necessarily the primary source of the energy radiated by SNe. Some SNe can be powered by other mechanisms, e.g. Type IIn SNe are thought to be powered by interaction with circumstellar material. Many powering mechanisms have been suggested for SLSNe [3].

Right after the explosion, the SN is in a dense, hot and optically thick phase. The material is so thick that the radiation escapes the ejecta slowly. The radiation is reprocessed by the material in the ejecta, making the SN radiation thermal. This means that the radiation is well described by the blackbody spectrum. The expansion of the ejecta allows the radiation to escape faster, i.e., the opacity decreases over time. Thus, even though most energy is released by the radioactive decay right after the explosion, SNe generally take days to weeks to reach its brightest moment.

For SNe that have radioactive decay as the primary source of radiation, ^{56}Ni decay is the dominant source of radiation when they are at their brightest. Due to the short half-life, the amount of ^{56}Ni is decreasing rapidly. Therefore, the decline rate of the light curve is fast compared to the tail phase when the ^{56}Co decay starts to be a significant contributor. ^{56}Co has a greater half-life, meaning the decay reactions happen less frequently but the amount of ^{56}Co also declines slower.

At $\sim$ 100-200 days after the explosion SNe enters the *nebular phase* in which the gas is optically thin and the radiation is not thermal anymore. The radiation at this phase is dominated by the emission lines. [4][5]

1.4 Stripped-envelope supernovae

Type Ib/c SNe lack hydrogen in their spectra. At the end of a typical stellar evolution cycle, the outermost layer of a star is hydrogen. The progenitors of Type Ib/c SNe must have lost their hydrogen envelopes before the explosion. In the cases of Type Ib SNe, there might remain a small hydrogen envelope, which can not be unambiguously identified in the spectra. Type IIb progenitors are believed to be stars that have lost a lot of hydrogen but not as much as Type Ib progenitors. Type IIb SNe progenitors still have clear hydrogen lines in their spectra. The threshold of hydrogen mass between Type Ib and IIb is ~ 0.03 $M_\odot$ [6][7]. Type Ic SNe progenitors have additionally lost their helium layers. Collectively Type IIb, Ib, and Ic SNe are called *stripped envelope supernovae* (SESNe). Figure 2 shows the composition of the progenitor stars of SESNe. [4]

The mechanism behind the stripping is a subject still under study. SNe progenitors are known to undergo radiation-driven mass loss. This mass-loss mechanism can further be boosted by the rotation of the star, which counteracts some of the gravitational pull on the surface of the star. Case studies of multiple Type Ib SNe have been conducted with radio observations, which have yielded estimates of pre-SN mass-loss rates of $10^{-5} - 10^{-4}$ $M_\odot$ yr^{-1} [8].

Wolf-Rayet (WR) stars seem suitable for the immediate progenitors of SESNe as they are just the kind of stars that have lost their hydrogen and, in some cases even helium envelopes. WR stars are believed to have lost mass through powerful stellar winds. Classical WR stars have ZAMS masses of $\gtrsim 35$ $M_\odot$ [4]. However, the rarity of WR stars does not match the rate of Type Ib/c SNe and case studies of Type Ib/c SNe have estimated the ejecta masses to be smaller than those of WR stars [9][10]. Evolutionary models of single stars have difficulty explaining the mass loss as extensive as in SESNe when the ZAMS masses are $\lesssim 25$ $M_\odot$ [11].

Figure 2 displays a schematic clarifying the structure of SESNe progenitors. In

binary systems, there is a region around the star called the *Roche lobe*, in which the material is gravitationally bound to the star. Should the star expand beyond the Roche lobe, the material beyond it will be ejected in the so-called *Roche-lobe overflow* [4]. The ejected material will be partially accreted by the companion star and partially ejected into the circumstellar medium. The amount of material lost in this manner depends mostly on the binary separation. The smaller the binary separation is, the greater the ejected fraction of hydrogen will be. The stars that have a close binary separation lose all or almost all of their hydrogen shell and become Type Ib SNe, whereas the stars with greater binary separations lose less hydrogen and become Type IIb SNe. The stars expand due to increased radiation pressure during later burning phases after the star exits the main sequence. Stars in binary systems with too great a separation will not fill their Roche-lobes and retain their hydrogen, eventually exploding as Type II SNe. Type Ic SNe come from helium-deficient stars. However, there is currently no generally accepted explanation for the loss of the He layer in these stars. According to theoretical simulations, binary systems with typical parameters do not expand enough to lose their entire helium envelope by binary interaction. The extreme cases in which this would be possible are not consistent with the rate of Type Ic SNe. [6] [12]

1.5 Interacting supernovae

Massive stars have CSM through line-driven wind but may have more dense CSM via some other mechanisms. Depending on the density of the CSM the *circumstellar interaction* (CSI) will be stronger or weaker. For strong CSI there are observable features in the light curve and spectra. These are henceforth called *interacting SNe*. The spectra of interacting supernovae might display narrow lines of the elements the CSM consists of. SNe interacting with dense hydrogen-rich CSM might have narrow hydrogen lines in their spectra.

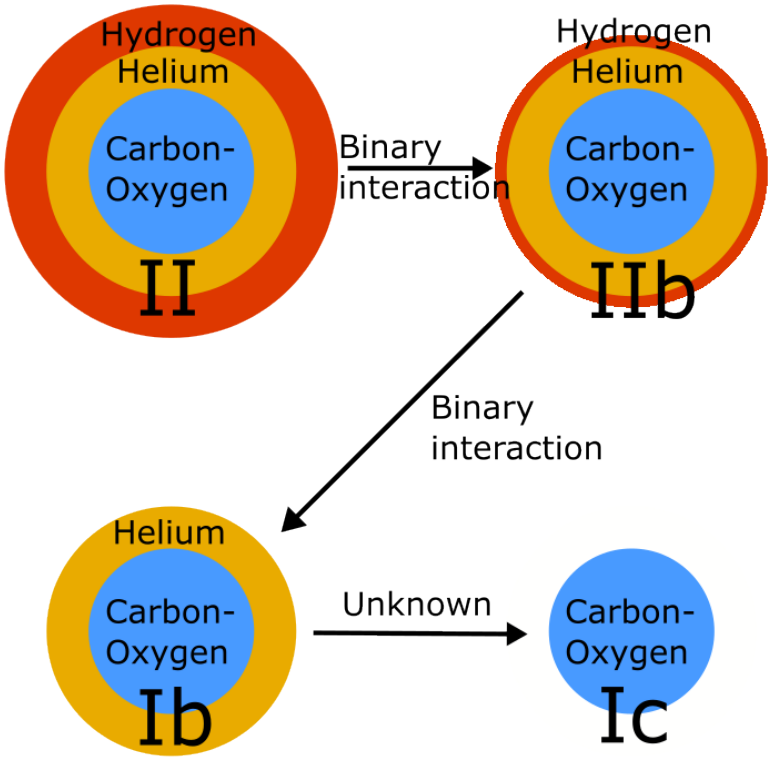

Figure 2. Progenitor stars of SESNe and the mass-loss mechanism that is thought to be responsible for the mass loss.

The observable features of interacting SNe are caused by the shock shell between the ejecta and the CSM. The ejecta velocity and density in the region of the interaction are orders of magnitude higher than that of the CSM. Upon collision between the ejecta and CSM, shocks are produced. The forward shock propagates outward in the unshocked CSM, accelerating and heating it. The reverse shock propagates inward in the unshocked ejecta, re-heating it. Between the shocked ejecta and the shocked CSM is the *contact discontinuity*. Complex hydrodynamical processes are happening around the contact discontinuity. See figure 3 for a schematic of a simplified interaction between a SN and CSM.

The unshocked CSM can be ionized by the interaction shocks. The recombination of these ions will cause narrow lines to be visible in the spectra. The unshocked CSM can also be ionized by the high-energy X-ray radiation originating in the interaction region. These features will be observable in the optical and UV spectra. The ejecta

will be slowed down by the collision with the CSM. The decrease in the velocity of the ejecta is too small to be directly measured from the spectra, however, a small part of the kinetic energy is transformed into radiation.

Typically light curves of SESNe are dominated by energy from ^{56}Ni decay and later from both ^{56}Ni and ^{56}Co decay. The radiation caused by the shock might become dominant over the radioactive decay if the CSI is strong enough. Even weaker CSI is usually observed in radio frequencies. Typical mass-loss rates inferred for SESNe with no strong interaction features are around$\sim 10^{-5}$ $M_\odot$ yr^{-1}. These mass-loss rates are likely due to line-driven wind. Greater mass-loss rates are found associated with Type IIn SNe, which have been shown to have mass-loss rates of up to $\sim 10^{-1}$ $M_\odot$ yr^{-1}. Some SESNe with strong CSI have been observed with various mass-loss rates and CSM chemical compositions.[8]

Depending on how long before the SN explosion the envelope was shed the SESN might have interaction features. If the mass was lost shortly before the explosion the light curve of the SN might have excess light manifesting in atypical light curve shape and potentially narrow emission lines in the spectra. However, if the envelope is lost sufficiently long before the explosion the CSM may be located too far away from the progenitor star for interaction to happen in the time scale of SNe. Whether the CSM consists of hydrogen, helium, or carbon and oxygen depends on the envelope the mass was most recently shed from. For example, Type IIn SNe interact with hydrogen, Type Ibn SNe and Type Icn SNe typically interact with He and C/O-rich CSM [4][13]. Typical values for mass-loss rate derived for SESNe correspond more with radiation-driven wind mass loss ($\lesssim 10^{-5}$ $M_\odot yr^{-1}$) rather than higher values that would be expected from binary stripping ($\gtrsim 10^{-5}$ $M_\odot yr^{-1}$) [8][12].

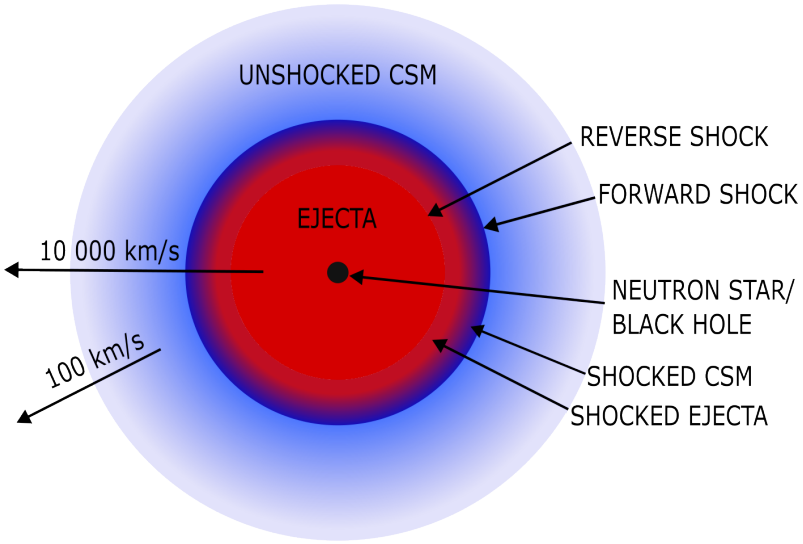

Figure 3. Schematic of the interaction between ejecta and CSM. The ejecta as well as the CSM might not in reality be spherically distributed. The CSM does not necessarily have a clear outer edge.

1.6 SN 2021efd

In this thesis, I present the observations of SN 2021efd, which is a peculiar Type Ib SN that has multiple peaks in its light curve. SN 2021efd was discovered on March 2. 2021 (MJD = 59275.8) with the Palomar 1.2m Oschin telescope by the Zwicky Transient Facility (ZTF) survey [14]. The last non-detection before the discovery was in the r band on MJD 59269.8. The host galaxy has a redshift of $0.027756 \pm 1.6{\cdot}10^{-5}$ [15], which corresponds to luminosity distance of 116.4 ± 0.1 Mpc with flat cosmology and Hubble parameter, H_0 value of 73 km s^{-1}Mpc^{-1} with $\Omega_{\mathrm{m}} = 0.3$ and $\Omega_\lambda = 0.7$. SN 2021efd was classified as a Type Ib by [16].

2 Observation

I present spectra of early and nebular phases of SN 2021efd as well as light curves observed by ZTF on g,r, and i bands and ATLAS o and c bands.

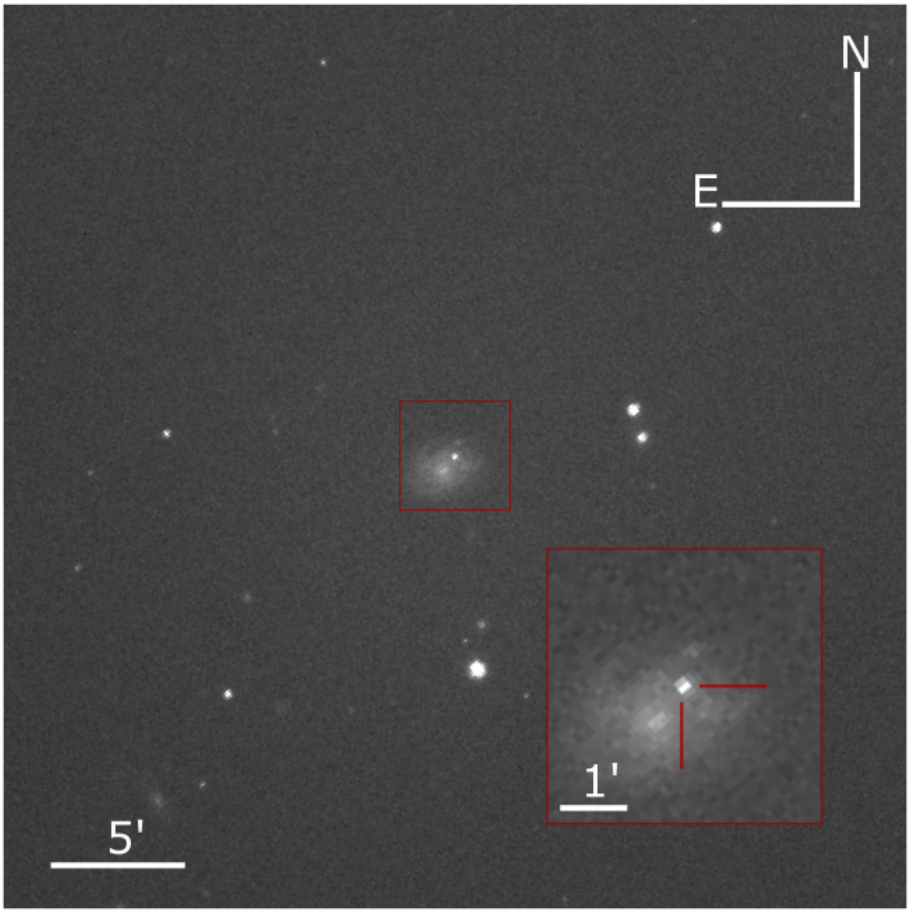

Figure 4. Acquisition image of SN 2021efd and the host galaxy. Image taken with the NOT telescope without filter on April 4. 2021 (MJD 59318).

2.1 Light curve

Photometric data of SN 2021efd were collected by ZTF[14] and ATLAS[17][18] surveys. The photometric data used in this thesis were acquired through ZTF Forced Photometry Service[1] and ATLAS Forced Photometry Service[2] respectively. Forced photometry means fitting a *point spread function* (PSF) on specified coordinates on an image. PSF describes how a point-like source appears when viewed through the atmosphere and the instruments. The PSF is determined from bright field stars in the image.

I combined the observations from individual nights into single data points. For

[1]https://ztfweb.ipac.caltech.edu/cgi-bin/requestForcedPhotometry.cgi

[2]Fallingstar-data.com/forcedphot/

ZTF forced photometry, I first placed the fluxes on the same zero point and a weighted average was counted with the equation $F = \frac{\Sigma_i w_i f_i}{\Sigma_i w_i}$, where f_i is the forced difference image flux of a single measurement and w_i determines how fluxes are weighted. The variable is defined as $w_i = \frac{1}{\sigma^2}$, where σ is the uncertainty of the flux measurement. The error of the combined binned flux is $[\sum_i w_i]^{-1/2}$.

I also combined the ATLAS observations of a single night. The presented magnitude is the average of all the measurements and the error is: $\frac{\Sigma \sigma_i}{n}$, where σ_i is the uncertainty of the magnitude and n is the amount of data points.

2.2 Spectra

Spectroscopic data were obtained on 5 different epochs. The four early-phase spectra were obtained with the *Nordic Optical Telescope* (NOT) using the *Alhambra Faint Object Spectrograph and Camera* (ALFOSC) instrument. The nebular phase spectrum was obtained with the *Very Large Telescope* (VLT) using the *FOcal Reducer and low dispersion Spectrograph 2* (FORS2) instrument. Spectroscopic data had been reduced with ALFOSCGUI and ESO pipeline for NOT and VLT spectra respectively. These perform bias reduction, flat-field correction, spectral extraction, wavelength correction, and flux calibration. The spectrum at the nebular phase had also been corrected for telluric features, i.e., absorption lines caused by the atmosphere.

3 Photometric properties

The multi-band light curve of SN 2021efd is displayed in figure 5. I corrected the light curve for galactic extinction $A_V = 0.052$ mag according to measurements reported in[19], which I acquired through the NASA/IPAC extragalactic database for the g, r, and i bands. Specific extinction measurements are lacking for the o and c

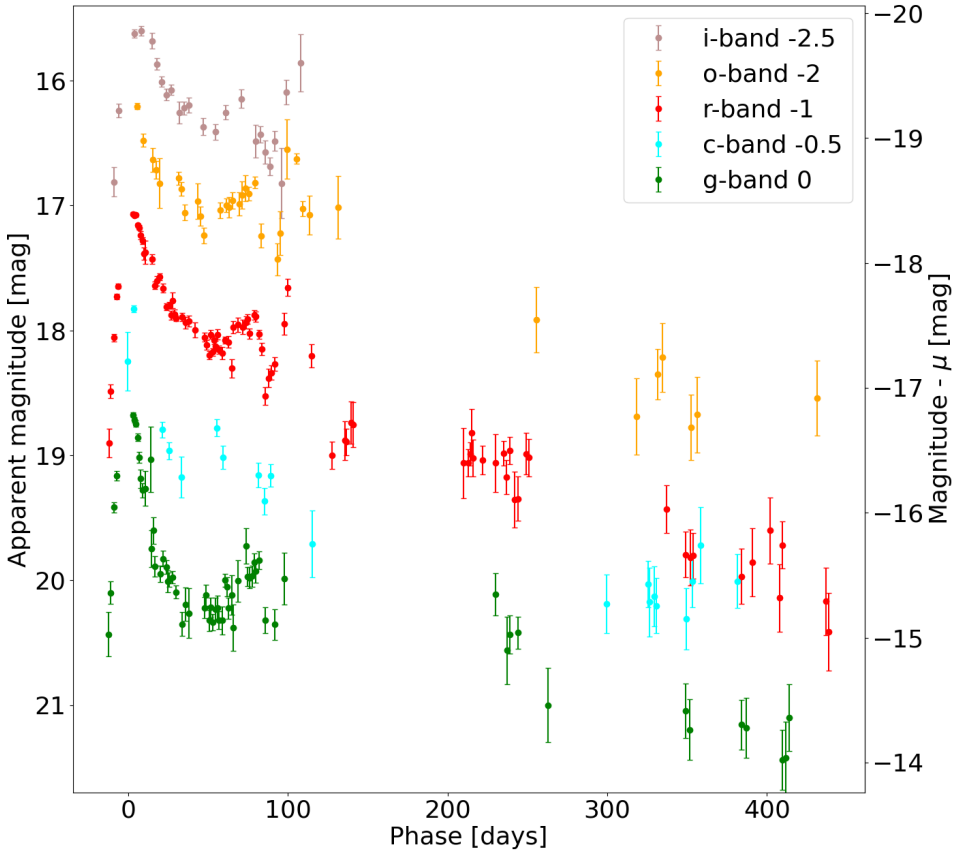

Figure 5. Light curve of SN2021efd on 5 different bands measured by 2 different surveys ATLAS and ZTF. Phases are relative to the assumed peak date of g-band. The variable μ is the distance modulus, 5 $\log_{10}(d/10\text{pc})$.

bands. Thus, I calculated the o and c band extinctions from the V band extinction according to extinction laws $\frac{A_o}{A_V}$ =0.773 and $\frac{A_c}{A_V}$=1.06 formulated in [20], which I acquired via SVO Filter Profile Service [21][22].

The early rise of SN 2021efd is not well observed. From the first detection, the light curve rises to the observed peak magnitude of $M_g = -16.7$ mag and $M_r = -17.3$ mag in $\sim$ 15 days. The light curve of SN 2021efd has a gap of $\sim$10 days before the first peak of the supernova on all bands except the i band.

3.1 Explosion date and rise time

From figure 5, it can be seen that on most of the bands, SN 2021efd was likely at its brightest during the gap before the observed peak magnitude. The first detection and last non-detection have 6 days between them. This together with an unknown peak date makes determining the rise time to the first peak a non-trivial task. The peak on the i band is reached later than on other bands. Because SNe are more commonly observed on g and r bands, determining the peak date from either of them allows a better comparison with other SNe. Since the interaction seems stronger on the redder bands, I determined the peak brightness on g band.

Due to its similar light curve shape in the early phase, iPTF13bvn can be used to estimate the peak date and the rise time of SN 2021efd. By assuming the rise time of SN 2021efd to be the same as for iPTF13bvn, I get the rise time of $\sim$17 days. The peak date of SN 2021efd was likely during the 10-day gap in observations around the peak. In order to determine the peak date I transform the V-band light curve of iPTF13bvn to g band and fit it to the g band light curve of SN 2021efd. I interpolated the observations of iPTF13bvn to match the epochs of SN 2021efd. I transformed the color according to the relation calculated in [23]. I performed the fitting by minimizing the χ^2 -value between the two light curves. This means I calculated the square of the vertical distance between the light curves of SN 2021efd and iPTF13bvn for every observation until $\sim$ 10 days after the peak of iPTF13bvn. I summed these values and then divided them by their amount yielding the χ^2 value:

$$\chi^2 = \frac{1}{n}\Sigma_1^n \frac{(M_{\mathrm{g,efd}} - M_{\mathrm{g,bvn}})^2}{\sigma_i^2}$$

where M_{g} is the magnitude, σ_i is the uncertainty of SN 2021efd's magnitude and n is the amount of observations of SN 2021efd. I only took the uncertainty in the magnitude of SN 2021efd into account because it is much greater than the uncertainty of the magnitude of iPTF13bvn. I then iterated through different possible

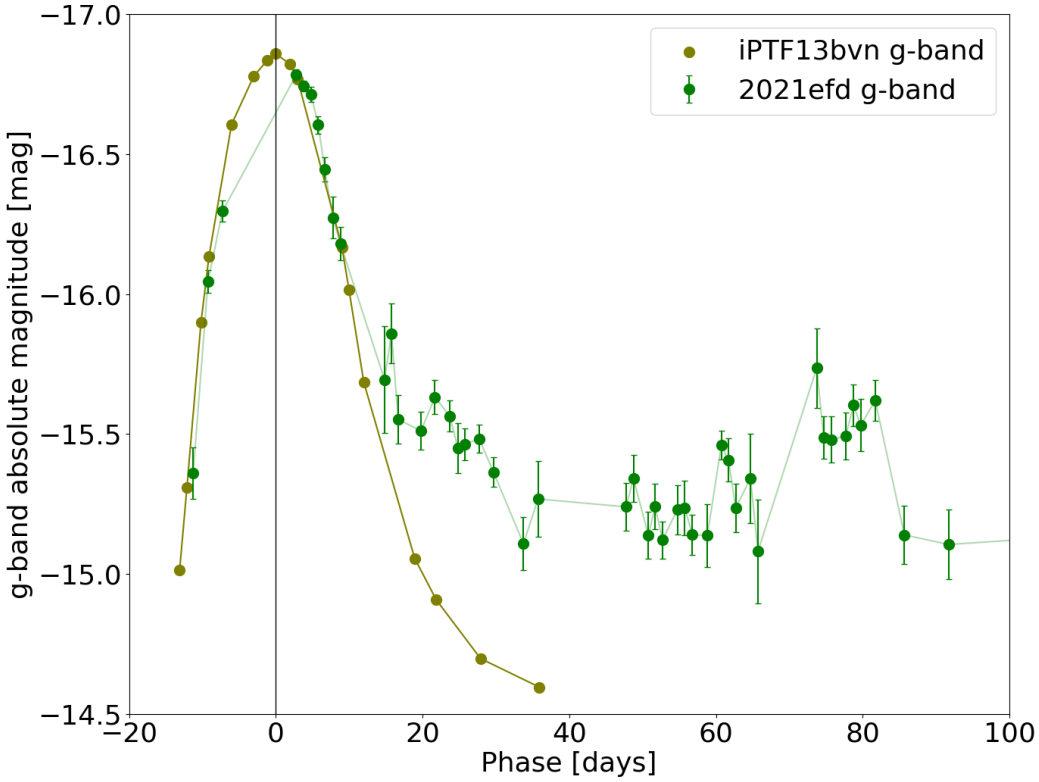

Figure 6. Light curves of iPTF13bvn and SN2021efd. The g band light curve of SN2021efd is fitted to match the color transformed V band of iPTF13bvn. The magnitude of iPTF13bvn is shifted in this image.

peak dates with the step of 0.01 days. I determined the peak date of SN 2021efd to be MJD 59288. From the rise time of $\sim$ 17 days, I estimate the explosion date to be MJD 59271. This is between the date of the last non-detection MJD 59269.8 and the date of the first detection 59275.7. The fit is presented in figure 6.

3.2 Light curve evolution

The light curve of SN 2021efd is bumpy with at least 3 peaks visible in the redder bands. After $\sim$ 100 days the photometric data becomes less frequent and the uncertainties increase. At $\sim$ 140 days SN 2021efd went behind the sun and was not observable for $\sim$ 70 days. The late phases of the light curve of SN 2021efd might

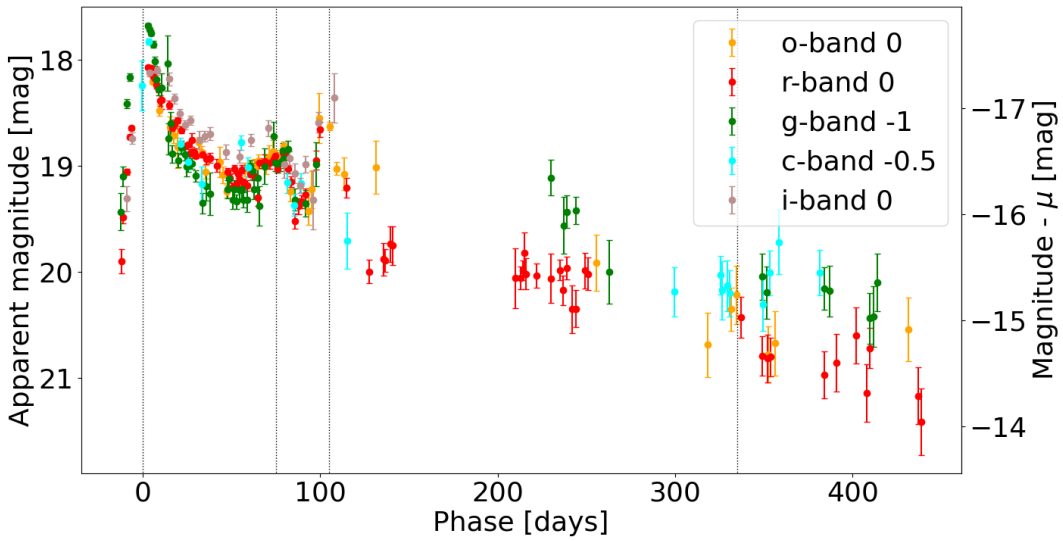

Figure 7. Light curves of SN2021efd. The observed magnitudes on different bands are shifted to roughly align during the second peak. The vertical lines highlight the peaks at $\sim$ 75 days, $\sim$ 105 days, and $\sim$ 335 days. The last of these peaks might be just noise. It is observed only on the o band and partially on the r band.

have more bumpy features that can not be distinguished with certainty because of the high uncertainties. The peaks are marked in figure 7.

I compared the light curve of SN 2021efd to light curves of SESNe in figure 8. The comparison SNe include a regular Type Ib SN iPTF13bvn [24], a regular Type IIb SN 1993J [25], a regular Type Ic SN 2007gr [26], and a peculiar Type Ib SN 2019tsf [14]. I also compare it to a Type Ib/c light curve template and a Type Ibn light curve template [27][28]. The peculiar SN 2019tsf exhibits multiple bumps in its light curve interaction features in its spectra but no hydrogen lines. It is thought to be interacting with hydrogen-poor CSM[29][30].

The rise rate of SN 2021efd before the first peak is similar to that of iPTF13bvn and higher than that of SN 2007gr. After the first peak, the SN decays at a similar rate to other Ib SNe light curves, meaning the first peak is likely due to ^{56}Ni-decay. Shortly after the first peak, the light curve begins a new rise to a second peak. The decay and subsequent new rise begin earlier on redder bands. The second peak is

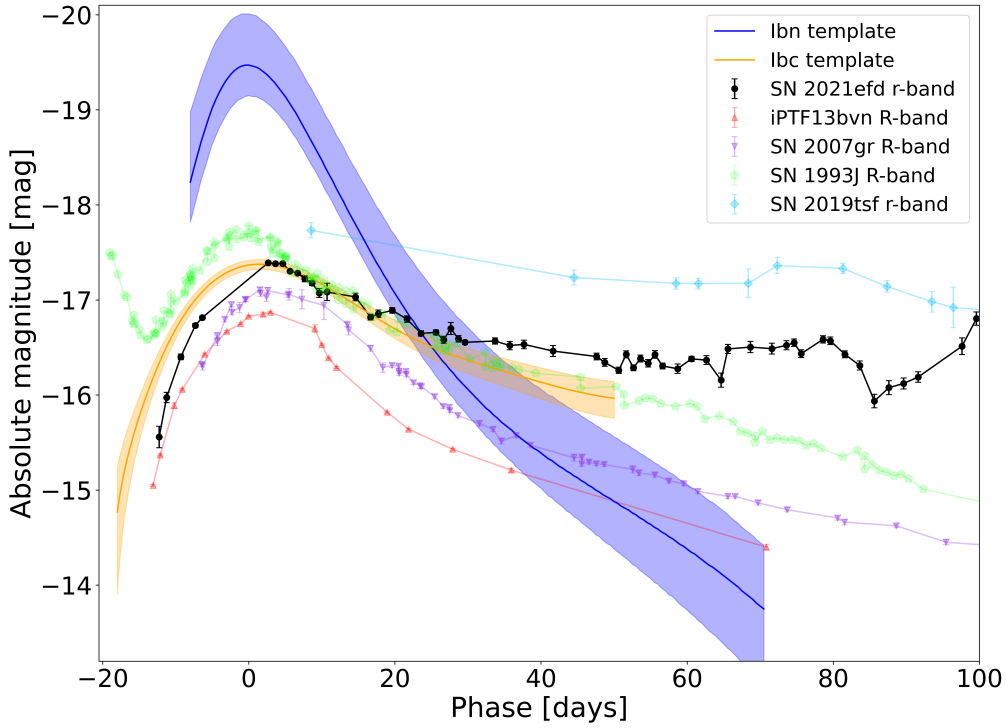

Figure 8. Comparison of the light curve of SN 2021efd with regular other SESNe and templates of Type Ibn SNe from [28] and Type Ib/c SNe from [27].

achieved at $\sim$ 70 days after the peak, which in the r, o, and i bands is followed by a new brighter peak $\sim$ 10 days after it.

The Type Ib SN iPTF13bvn, Type IIb SN 1993J, and Type Ic SN 2007gr have similar rise and decline rates near the first peak. By comparing SN 2021efd to iPTF13bvn on the r band, it can be seen that the re-brightening of SN 2021efd begins at $\sim$ 30 days after the first peak. The similarities of SN 2021efd with regular Type Ib and IIb SNe end at this time. SN 2019tsf, which is interpreted to be a Type Ib SN interacting with He-rich CSM [29][30], has a similar bumpy light curve with excess energy that can not be explained by ^{56}Ni-decay.

I also compared SN 2021efd to the Type Ibn SN light curve template presented in [28] and the of Type Ib/c SN template presented in [27]. The Type Ibn template is the average R band magnitude of the Type Ibn SNe in the sample presented in

the same article. The template for Type Ib/c SNe is the average of the SNe light curves in the sample after they were scaled with peak magnitude. In other words, the Ib/c light curve template describes the typical rise and decline rate of the SNe, ignoring differences in peak magnitude. I scaled this template with the peak of SN 2021efd in figure 8.

The color evolution of SN 201efd is presented in figure 9. I compared the color evolution to the templates presented in [31]. I corrected the color evolution of SN 2021efd to match the *V*-*r* bands of the templates. I used the g and r bands, which I interpolated to match epochs. I calculated the color correction according to the transformation equation presented in [23]. The evolution of the color of SN2021efd is similar to those of the SESNe templates, but redder across all epochs. At $\sim$ 100 days, the uncertainties in the photometry of SN 2021efd become large and observations on different bands do not always coincide. The color jumps to a much bluer value at $\sim$ 100 days. This aligns with the gap in observations due to SN 2021efd going behind the sun and might not be a real jump. The apparent blueness of SN 2021efd might be due to CSI. It might also be due to underestimating the extinction. However, the extinction from the host galaxy is assumed to be small due to the lack of sodium absorption lines in the spectra and the extinction of the Milky Way has small uncertainties. Another possible explanation is that the transformation law used does not work well on SNe.

3.3 Bolometric light curve

I derived the bolometric light curve and the evolution photosphere radius and temperature for SN 2021efd. The bolometric light curve is the radiation across all wavelengths plotted over time. To create a bolometric light curve, I fitted the blackbody function to the light curve data from different wavelength bands. Each flux measurement from observations needed to be changed into the specific intensity at

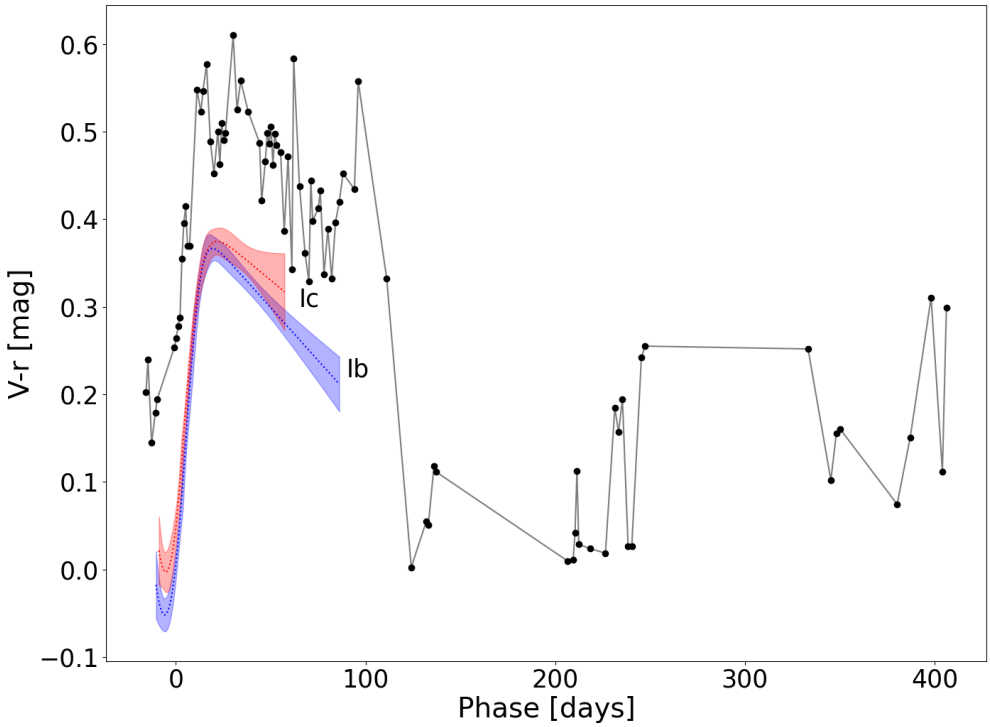

Figure 9. Color evolution of SN 2021efd. The templates in the figure are those of Type Ib SNe and Type Ic SNe SNe presented in [31].

the filter's effective wavelength. The effective wavelength is the average wavelength in the filter's range weighted by the transmission of the standard star, Vega through the filter function. I transformed the flux measured through the filter into intensity by dividing the flux by the effective width of the filter. The effective width of the filter is the width of a rectangle that has the same area and maximum transmission of the filter.

Essentially the filter is assumed to be a rectangle, the flux is divided by its width, and the resulting intensity is assumed to be the intensity of the blackbody function at the center of the filter.

To account for the distance of the SN, I transformed the blackbody function into flux by dividing it by $4\pi d^2$, where d is the distance to the SN.

To create this fit, measurements with multiple bands were needed, since fitting

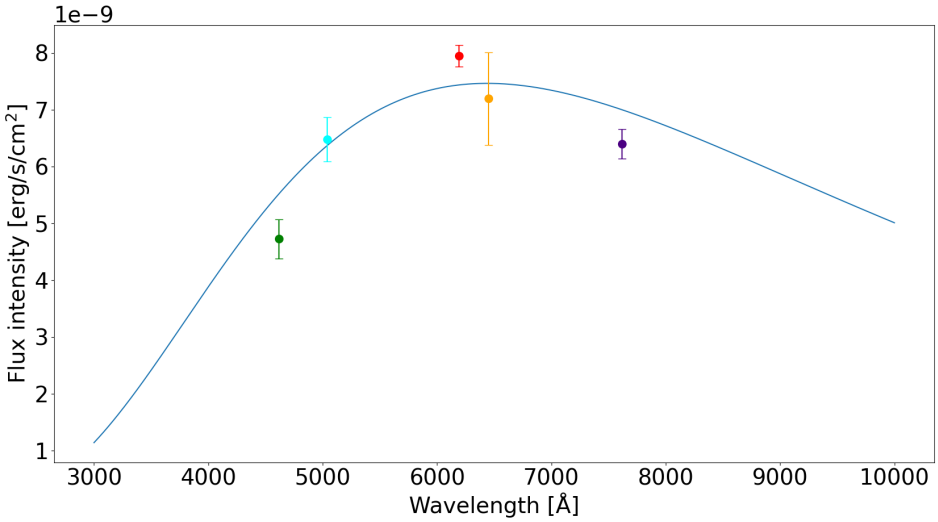

Figure 10. Blackbody fit through flux measurements with 5 filters, ZTF *g*, *r*, *i* and ATLAS *o* and *c*. This fit is from 25 days after the first peak.

a curve through measurements only at one or two wavelengths does not capture the shape of the curve. I interpolated the measurements for each day between the first and last measurements in every band. All five bands have measurements from before the first peak up to 104 days after the peak. I performed the fitting with the χ^2 method. The χ^2- method is explained in 3.1. An example of the best fit 25 days after the peak is in figure 10. I calculated the χ^2 values systematically with all reasonable radius and temperature values ($2000-9000$ K and $10^{14}-5\cdot10^{15}$ cm) with steps of 50 K and 10^{13} cm respectively. Once I had acquired the photosphere radius and temperature until the nebular phase, I calculated the luminosity of the SN with Stefan-Boltzmann law $L = 4\pi R^3 \sigma_{\mathrm{SB}} T_{\mathrm{eff}}^4$. Errors for the χ^2 fit are typically expressed as the confidence interval. The 1-σ region is $\chi^2 \pm \Delta\chi^2$, where $\Delta\chi^2$ is determined by the number of different bands that were used. I used the largest and smallest values of temperature and radius that are within $\Delta\chi^2$ from χ^2 as the error for the plots of radius and temperature. Similarly, the error of bolometric luminosity is the smallest and largest values plugged into the Stefan-Boltzmann law.

In figure 11, the bolometric light curve and the temperature and the radius

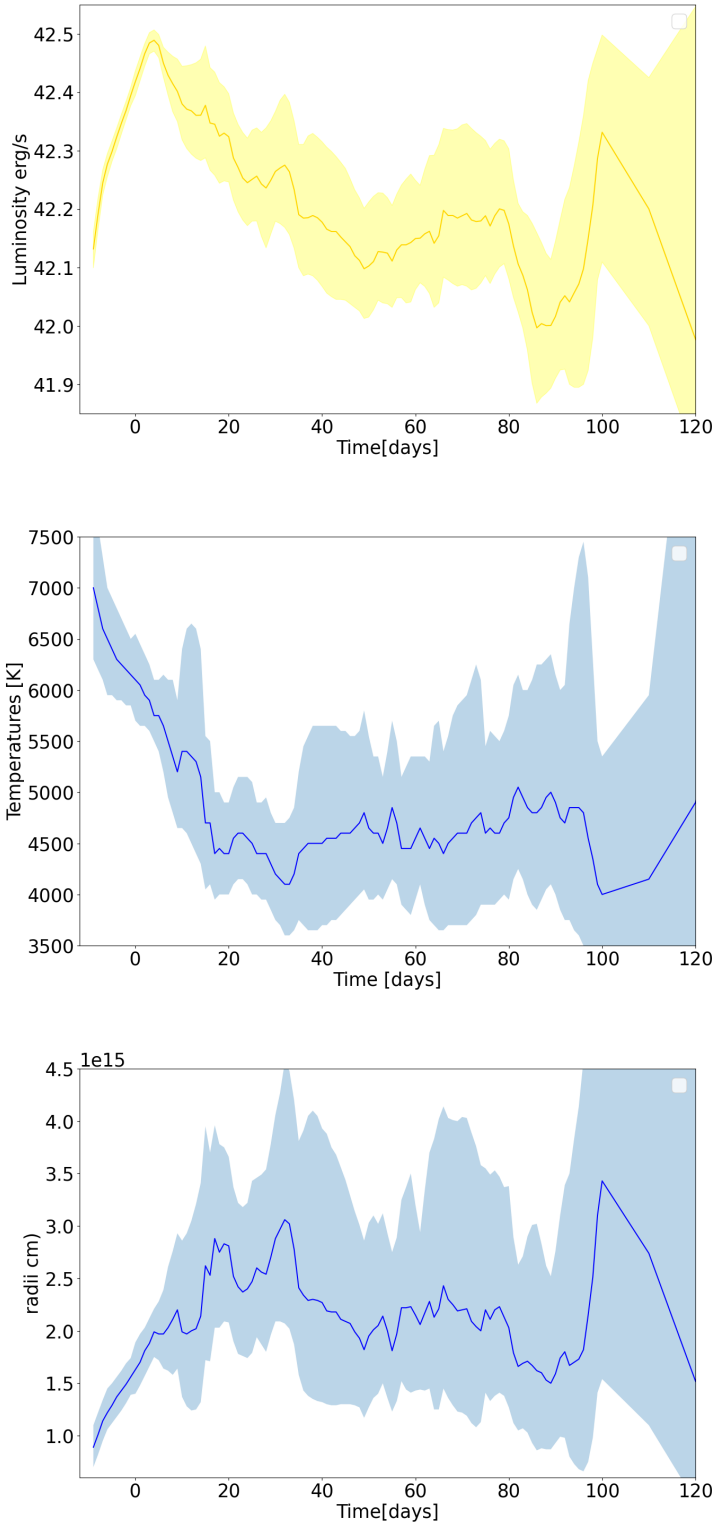

Figure 11. Results of the SED fitting. Top: the bolometric light curve of SN 2021efd. Center: Temperature of the photosphere. Bottom: Radius of the photosphere. The errors for all three plots are the 1-σ values of the χ^2-fitting. At the late phase $\gtrsim 100$ days the photosphere becomes optically thin and the blackbody fit becomes less accurate hence the great error bars at late epochs.

evolution of the photosphere are plotted until 120 days after the peak. As can be seen in the figure the uncertainty rises greatly after $\sim$ 100 days. The uncertainty of the fit increases due to increased uncertainty in the photometry at late phases. The assumption that the SN radiation is well described by a blackbody is only accurate at the early phase. As the ejecta expands it becomes optically thinner. Eventually, it can not be described by the blackbody function anymore. Instead, the spectrum is dominated by strong emission lines. After $\sim$ 120 days the 1-σ limit for the χ^2 fit becomes so large that the free parameters can not be constrained by the χ^2 fitting method. The results of the fitting at all phases are displayed in Appendix A.

4 Spectroscopic properties

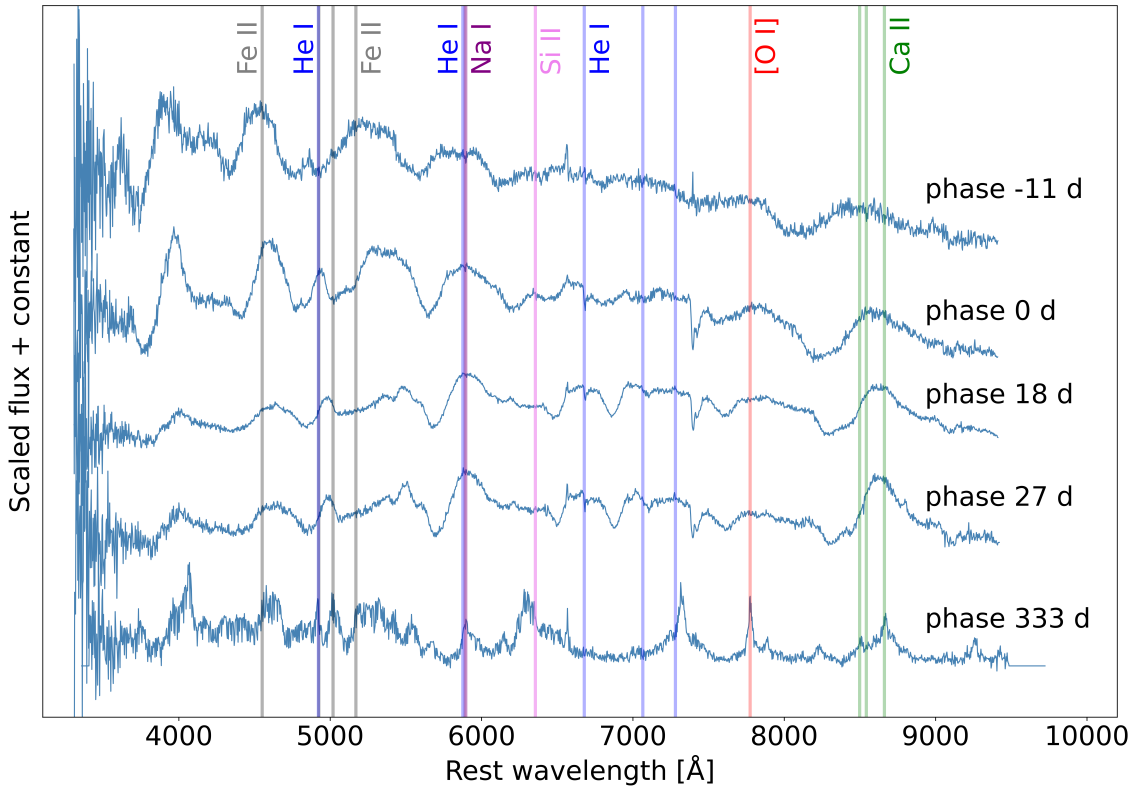

Figure 12. Spectra of SN2021efd from five different phases.

Spectra of SN 2021efd are displayed in figure 12. Spectra of SN 2021efd has helium lines at 5876 Å and a weak Si II absorption line at 6150 Å. No hydrogen is present at 6563 Å. These features confirm the original classification of SN 2021efd as Type Ib SN [16]. In figure 13, I compare SN 2021efd to other SNe. I chose a regular SN from each SESNe subtype, Type Ib iPTF13bvn, IIb SN 1993J, Ic 2007gr. The epochs of the spectra are as close to the peak date as possible. From these comparisons, it can be seen that SN 2021efd most closely resembles the Type Ib iPTF13bvn. In addition, I compare SN 2021efd to the interacting Type Ib SN 2019tsf. The Si II absorption line at 6355 Å is stronger in SN 2021efd and so is the He I line at 5876 Å.

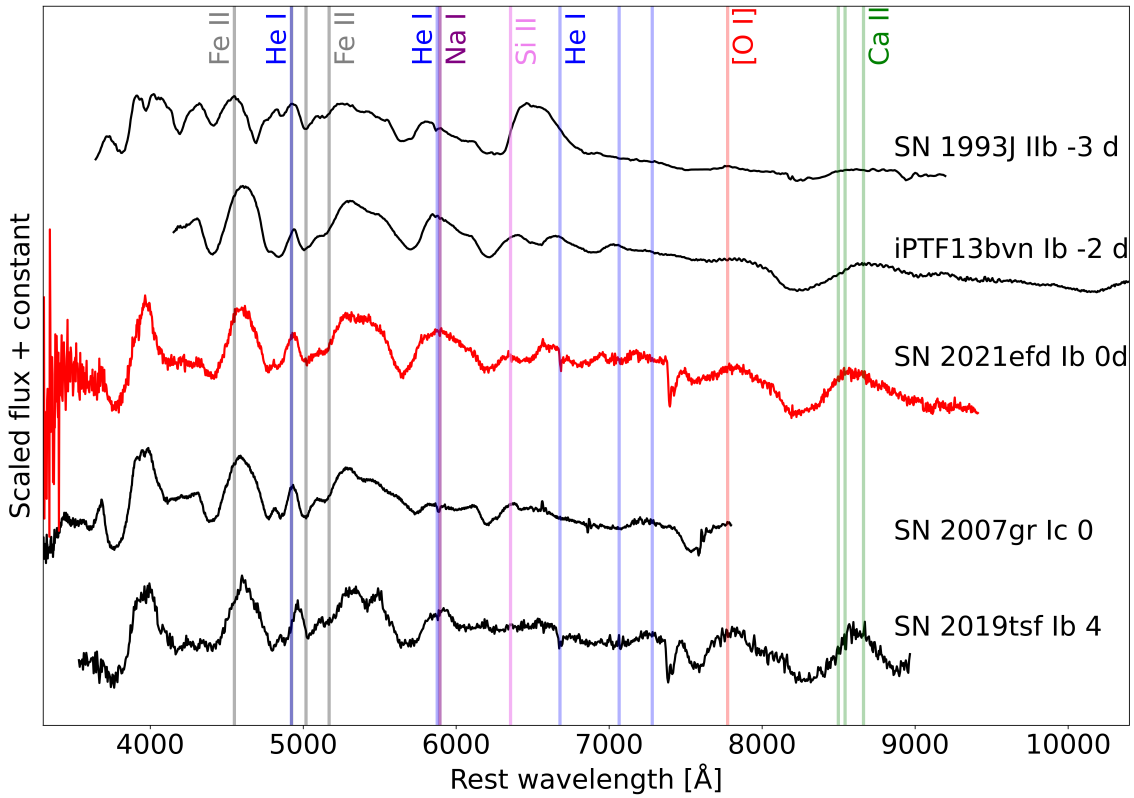

Figure 13. The nebular phase spectra of multiple SESNe and SN2021efd. Normalization was done by dividing the flux of every wavelength by the peak flux between $4200 - 5000$.

In figure 14, I compare SN 2021efd to the nebular phase spectra of other SNe. The comparison SNe are the same as for the early phase comparison. Compared

to iPTF13bvn, which is very similar in the early phase, the nebular phase of SN 2021efd has a much stronger near-infrared (NIR) Ca II triplet feature in its spectra. The nebular phase spectra of SN 2021efd seems to have narrow lines on top of the usual broad lines. As discussed in chapter 1.5, they are common in interacting SNe. It also has *Lorentzian wings* in its nebular lines, i.e., rather than a Gaussian line shape the base of the line has a Lorentzian profile. The Lorentzian features are likely caused by photon scattering from CSM and are typical in interacting SNe (eg. [32][33]). The region around the iron complex at $\sim$ 5200 Å appears to have a higher baseline flux in the spectra of SN 2021efd and the interacting SN 2019tsf compared to the regular SESNe. This is a feature commonly observed in interacting SNe (e.g.[34],[35]).

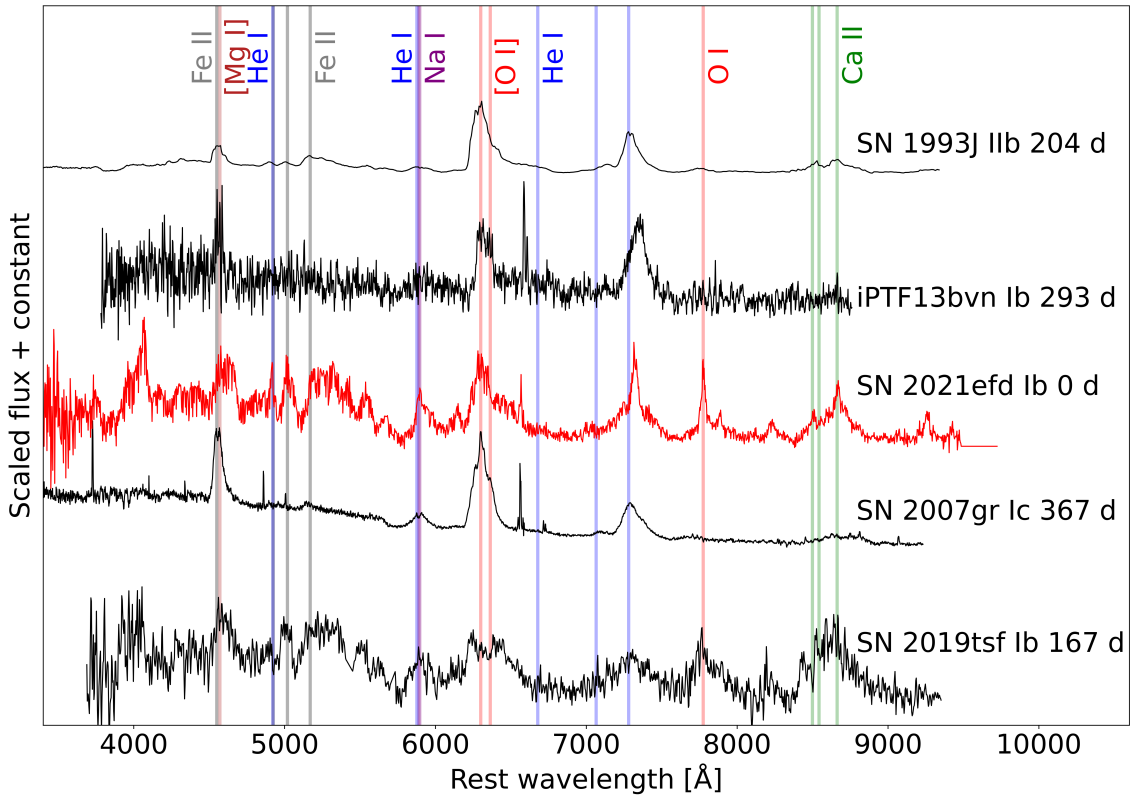

Figure 14. The nebular phase spectra of multiple SESNe and SN2021efd. Normalization was done by dividing the flux of every wavelength with the peak flux around the Ca II line at $\sim$ 7200 .

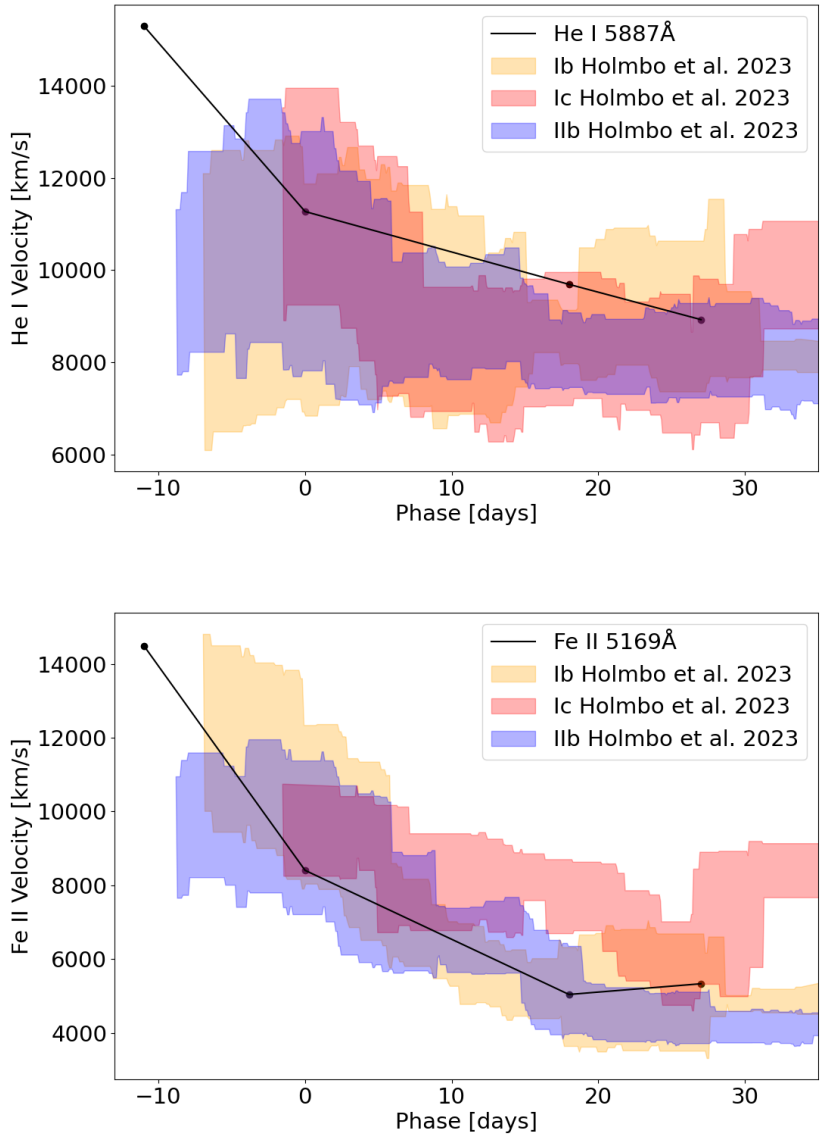

Figure 15. Photosphere velocity evolution of SN 2021efd over 4 epochs. The templates on the background were presented in [36].

4.1 Velocity evolution

I calculate the ejecta expansion velocity from the He I 5876 Å line and the Fe II 5169 Å lines in the early phase spectra. The velocity is $v = \frac{\Delta\lambda}{\lambda_r}c$, where λ_r is the rest wavelength, c is the speed of light, and $\Delta\lambda$ is the difference between absorption minima and rest wavelength. I determined the wavelength of the absorption minima

by fitting a Gaussian profile to the line with the splot tool in IRAF.

In figure 15 I compare the expansion velocity of SN 2021efd to templates of expansion velocities. The template in the figure is the standard deviation of the rolling mean of the sample of SESNe presented in [36]. The He I expansion velocity of SN2021efd is on the higher end of what is typical for SESNe. The Fe II expansion velocity is on the lower end of what is typical for SESNe.

5 Supernova properties

5.1 Ejecta mass and Kinetic energy

Despite massive amounts of energy ($\sim 10^{51}$ergs) being released at the moment of the explosion, it takes a few weeks for a SN to reach its brightest moment. The explosion deposits kinetic and thermal energy to the SN ejecta. The ejecta is radiation-dominated gas. Diffusion time refers to the average time for a photon to find its way past the photosphere and escape. The diffusion time is proportional to the opacity of the ejecta. The scattering of photons from free electrons, i.e., Thomson scattering is the main source of opacity. Another source of opacity is line absorption by atoms; this is the source of the absorption line in the spectra. The absorbed photons are re-emitted at other wavelengths. Diffusion time is very long early on, which means the moment of the explosion is not yet the brightest moment of the SN. [4] Diffusion time of a photon: [37][38]

$$t_{diff} = \frac{\kappa M}{\beta c R}$$

In the equation above, κ is the mean opacity in ultraviolet, optical, and infrared. Here κ is assumed to be 0.1 cm^2 g^{-1}, which is typical for ionized gas [4]. M is ejecta mass, β is an integration constant that has a value of 13.8, c is the speed of light, and R is the photosphere radius of the SN. Because the ejecta is expanding, the radius increases over time. This means that diffusion time decreases over time.

To judge when the luminosity of a SN reaches its peak, we have to know the timescale of the ejecta's expansion. The *hydrodynamic timescale* represents this:

$$t_h = \frac{R}{v_{sc}}$$

Velocity here is *scale velocity*, which is the velocity of ejecta at distance R. Taking R as the radius of the photosphere we can identify v_{sc} as v_{ph}, i.e., the velocity of the photosphere.

Through a complex calculation, these two timescales can be combined to the *effective time* of a SN [37][38]:

$$t_{eff} = \sqrt{2t_{diff}t_h} = \left(\frac{2\kappa M}{\beta c v_{ph}}\right)^{\frac{1}{2}}$$

Models show that this timescale is closely related to the rise time t_{max} of SNe [39]. The mass M here refers to the mass that affects diffusion time and not the non-ionized matter. However, this yields a good estimate of the ejecta mass. [4]

$$M_{\rm ej} = \frac{1}{2}\frac{\beta \rm c}{\kappa} v_{ph} t_{\rm max}^2 \tag{1}$$

The classic relation for ejecta mass and kinetic energy of the ejecta applies here $< v^2 >= \frac{2E_k}{M}$. However, the velocity of the photosphere can not be taken for the velocity of the ejecta. The average velocity of the ejecta is related to the photosphere velocity by $v_{ph}^2 = \frac{5}{3} < v^2 >$, assuming homologous expansion with constant density in every part of the ejecta. Now, these equations can be plugged into the equation above and the equation can be inverted to give the kinetic energy of the ejecta.

$$E_k = \frac{3}{20}\frac{\beta \rm c}{\kappa} v_{ph}^3 t_{\rm max}^2$$

The expansion velocity was measured in chapter 4.1. I assume the expansion velocity of Fe II 5169 Å line at peak to be the photosphere velocity and the rise time to be the same as for iPTF13bvn. I calculate the kinetic energy and the mass of ejecta. The ejecta mass of SN 2021efd is 2.18 $M_\odot$ and the kinetic energy of the

ejecta is $1.2 \cdot 10^{51}$ ergs. These values are close to those estimated for iPTF13bvn [24].

5.2 Progenitor mass

The progenitor masses of SESNe have been shown to have a correlation with the [O I]/[Ca II] flux ratio in nebular spectra[40]. It does not prove a direct measure of progenitor mass as the [O I]/[Ca II] ratio does not depend solely on progenitor mass but on other parameters as well. However, it can be used as a rough estimate of the progenitor mass. I estimated the progenitor star mass of SN 2021efd from the [O

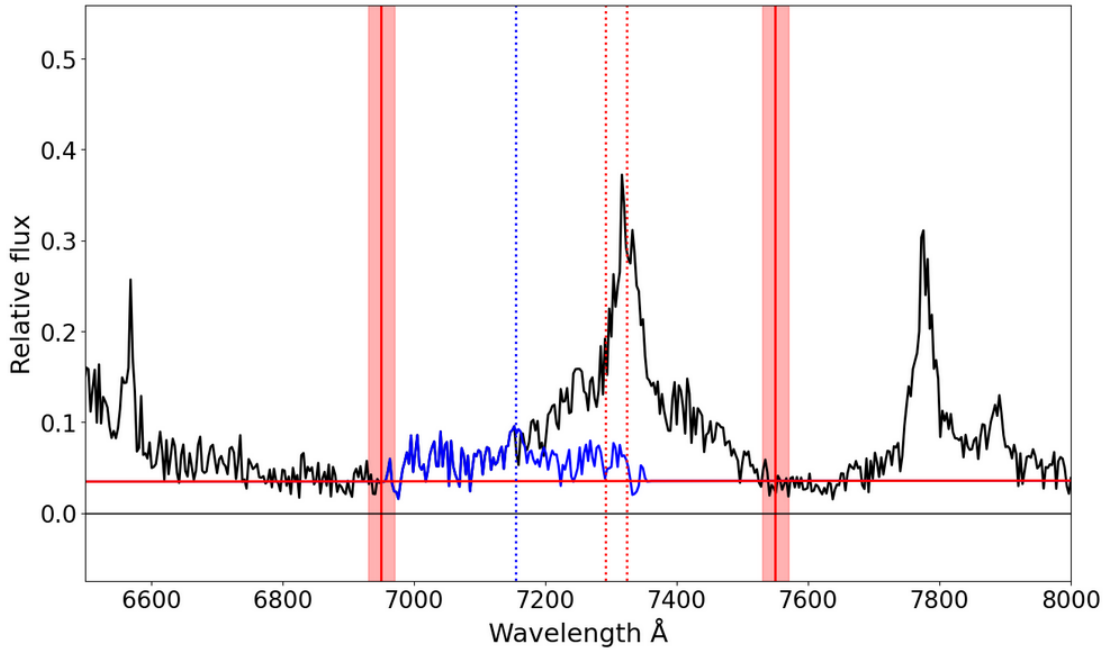

Figure 16. [Ca II] doublet of SN 2021efd. The blue dotted line marks the rest wavelength of the nearby [Fe II] line at 7155 Å and the red dotted lines are the rest wavelengths of the Ca II lines. The flux on the left side of this line is assumed to be solely due to [Fe II] and the line is assumed to be symmetrical. The total line is then subtracted from the [Ca II] line. The red borders define the area integrated over. The baseline is drawn between the average flux in the 20 Å range around the borderline. This is the horizontal red line at the bottom.

I]/[Ca II] ratio of the nebular spectra. I measured the fluxes [O I] 6300/ 6364 Å and [Ca II] 7292/7324 Å doublets of SN 2021efd by integrating the area under the curve

from the approximated area of the line. For this, I placed left and right borders where the spectrum seems to be at the continuum level. Both the [O I] and the [Ca II] doublets are near [N II] and [Fe II] lines respectively. In order to not overestimate the flux intensities I subtracted these lines. See figure 16 for clarification.

The [O I]/[Ca II] ratio I measured for SN 2021efd is 1.3. This number is affected by uncertainties from the nearby lines, in particular their possible asymmetry. I compare modeled spectra of SESNe in [41]. These models are created for varying initial conditions including mass. I measured the [O I]/[Ca II] ratio for these models with the same method. I chose the models in the phases closest to the nebular spectra of SN 2021efd. The results are plotted in figure 17. The [O I]/[Ca II] ratio of SN 2021efd is near those of the models where the helium star mass was 7 $M_{\odot}$, which corresponds to *zero age main sequence* (ZAMS) mass of ~ 25 $M_{\odot}$ [41][42][43].

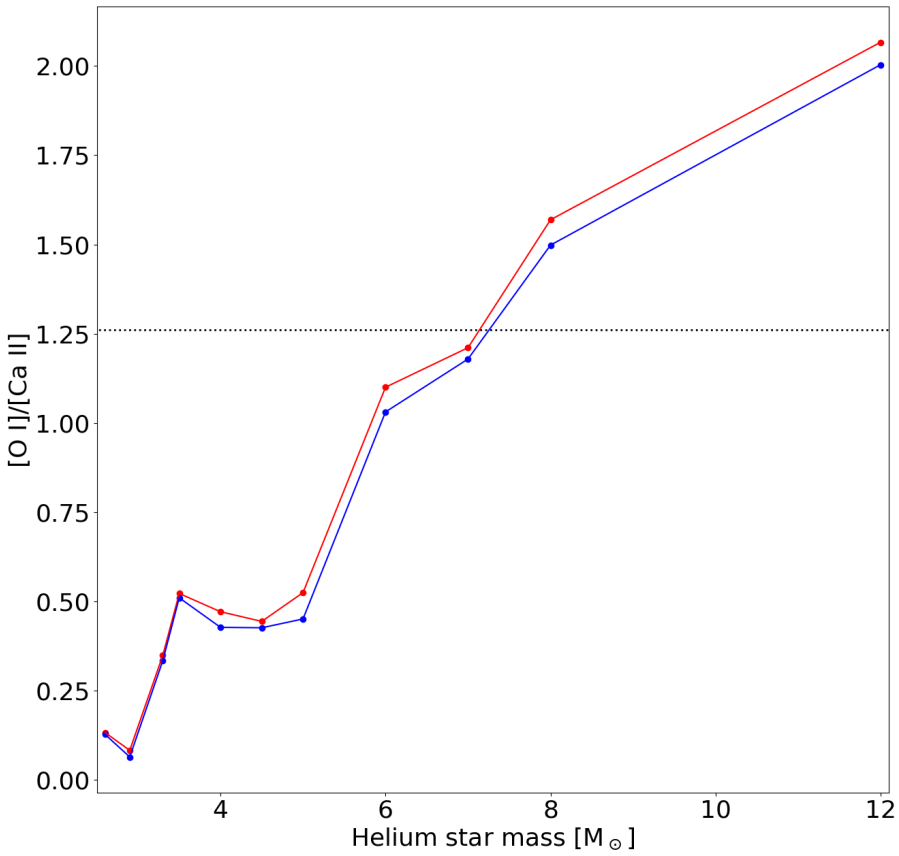

Figure 17. [O I]/[Ca II] ratio of models for different helium star masses measured synthetic spectra presented in [41]. The red dots are the ratio of the models at 320 or 322 days from the explosion and the blue dots of models at 340 or 354 days. The black dotted line is the [O I]/[Ca II] ratio measured for SN 2021efd. The [O I]/[Ca II] ratio of SN 2021efd corresponds to the ratio of the models with helium star mass of ~ 7 $M_{\odot}$.

6 CSM properties

6.1 Interaction model

The interaction between the SN ejecta and the CSM creates a shock shell consisting of the forward shock and reverse shock, as discussed in Chapter 1. For the following model, it is assumed that the physical parameters are uniform within the shock shell, and its width is also assumed to be insignificant in comparison to its radius. The *equation of motion*, (EOM) of the shock shell is [44][45]:

$$M_{\rm sh}(r_{\rm sh},t)\frac{{\rm d}v_{\rm sh}}{{\rm d}t} = 4\pi r_{\rm sh}^2\left[\rho_{\rm ej}\left(v_{\rm ej}-v_{\rm sh}\right)^2-\rho_{\rm csm}\left(v_{\rm sh}-v_{\rm w}\right)^2\right], \tag{2}$$

where ρ is density and the subscripts sh, ej, and w represent shock shell, ejecta, and wind, respectively. The wind velocity is assumed to have been constant over the mass loss period. The ejecta velocity is $v_{\rm ej}(r) = \frac{r}{t}$. The density of the CSM at r is:

$$\rho_{\rm CSM}(r) = \frac{\dot{M}}{4\pi r^2 v_{\rm w}}, \tag{3}$$

where $\dot{M}$ is the mass-loss rate of the progenitor star. The mass-loss rate is assumed to have been constant.

In the EOM, the mass and acceleration are on the left side of the equation, and the right side shows the force as a function of velocities and densities of different components. The velocity differences of the shock shell to ejecta and CSM multiplied by the densities on each side of it are the ram pressures toward the shock shell from each side. In other words, the squared difference between the ejecta velocity and the shock shell velocity causes pressure on the shock shell surface, which scales with the density of the ejecta. In the same way, the squared difference of the CSM velocity to the shock shell velocity causes a pressure inward that scales with CSM density. These pressures cause a force that depends on the surface area in question. The density profiles of the ejecta are based on numerical simulations and are assumed to

follow a double power law distribution [45]:

$$\rho_{\rm ej}\left(v_{\rm ej},t\right)=\begin{cases}\frac{1}{4\pi(n-\delta)}\frac{\left[2(5-\delta)(n-5)E_{\rm ej}\right]^{(n-3)/2}}{\left[(3-\delta)(n-3)M_{\rm ej}\right]^{(n-5)/2}}t^{-3}v_{\rm ej}^{-n} & \left(v_{\rm ej}>v_t\right),\\ \frac{1}{4\pi(n-\delta)}\frac{\left[2(5-\delta)(n-5)E_{\rm ej}\right]^{(\delta-3)/2}}{\left[(3-\delta)(n-3)M_{\rm ej}\right]^{[\delta-5)/2}}t^{-3}v_{\rm ej}^{-\delta} & \left(v_{\rm ej}<v_t\right),\end{cases} \tag{4}$$

where v_t is the velocity at the border of the power laws. Solving this EOM at $r=r_{\rm sh}$ yields the distance and the velocity of the shock shell as a function of time. This equation can be analytically solved only until time t_t when $v_{\rm ej}=v_t$, i.e., the density profile changes power laws [45]:

$$t_t=\left[\frac{v_{\rm w}(3-s)(4-s)}{\dot{M}(n-4)(n-3)(n-\delta)}\frac{\left[(3-\delta)(n-3)M_{\rm ej}\right]^{(5-s)/2}}{\left[2(5-\delta)(n-5)E_{\rm ej}\right]^{(3-s)/2}}\right]^{\frac{1}{3-s}}, \tag{5}$$

where $E_{\rm ej}$ and $M_{\rm ej}$ are the kinetic energy of the ejecta and the ejecta mass respectively. The values, inner density slope δ, outer density slope n, and CSM density slope s describe the density profile of the system. After t_t I solved the equation numerically using the Runge-Kutta method. More details on the Runge-Kutta method and its application here are in Appendix B or in [46].

In addition to the velocity evolution of the shock shell, the luminosity evolution of the interaction can be calculated. In the shock shell, kinetic energy is transformed into radiation with some efficiency. This is high energy radiation some of which will be re-processed by the dense material to blackbody radiation near the optical light. By combining these effects we get the efficiency ϵ, which is the efficiency of the transformation of kinetic energy into radiation.

$$L=\epsilon\frac{{\rm d}E_{\rm kin}}{{\rm d}t}=2\pi\epsilon\rho_{\rm csm}r_{\rm sh}^2v_{\rm sh}^3 \tag{6}$$

The CSM expansion velocity can not be constrained for SN 2021efd because there are no observed lines from the unshocked CSM in the spectra. The value I used for the CSM velocity is $v_{\rm w}=100$ km s^{-1}, which is a typical velocity of winds in luminous blue variables [47]. I used the values $n=10$, $\delta=1$, and $s=2$. The value $s=2$ refers to the steady mass loss scenario of pre-SN mass loss. I assumed

the value of ϵ to be 0.1. This value can not be determined for SN2021efd with good accuracy thus I used an order of magnitude estimation from [48] based on Type IIn SNe.

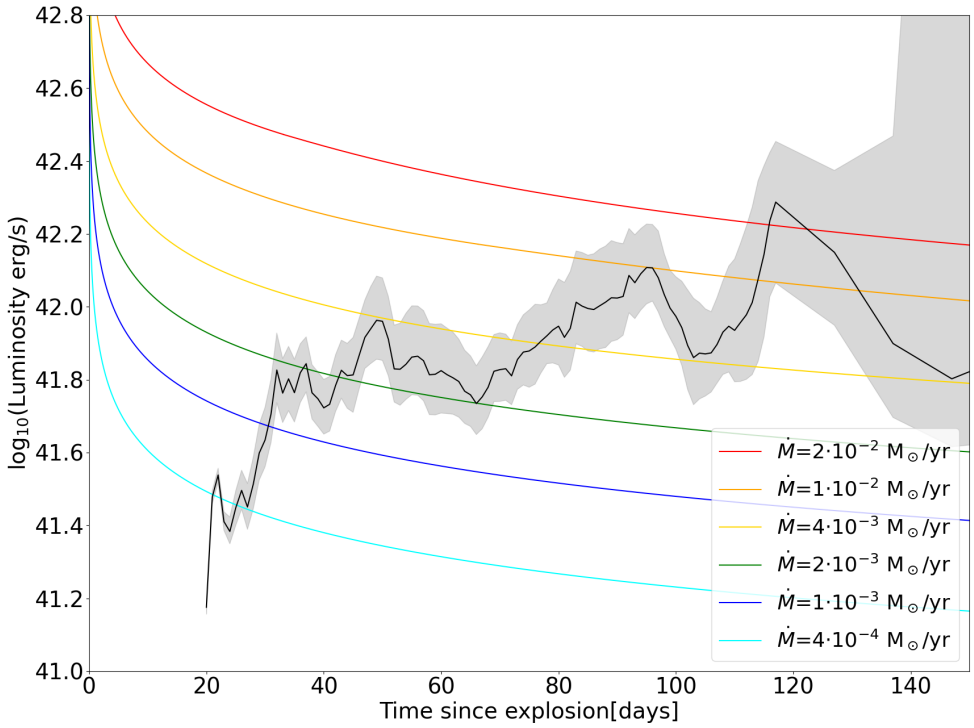

Figure 18. Colored lines: the calculated radiation from interaction with different mass-loss rates. The black line is the bolometric light curve of SN 2021efd derived in 3.3 with the SN component subtracted out.

The bolometric light curve is compared to the calculated interaction luminosity in figure 18. The bolometric light curve has the *SN component* removed. This means that from the bolometric light curve of SN 2021efd, I subtracted the average bolometric light curve of Type Ib SNe. The bolometric light curves I chose were of SNe with no significant peculiar features. The average was calculated from 9 bolometric light curves presented in [27]. I scaled the bolometric light curves by dividing the flux at every phase by the peak magnitude. I scaled this average flux to match the peak bolometric luminosity of SN 2021efd. Assuming these SN were

primarily powered by radioactive decay, the resulting bolometric light curve should represent the interaction powered luminosity in SN 2021efd.

From $\sim$ 30 days after the explosion onward, the interaction luminosity is steadily increasing. This could be due to a slow increase in mass-loss rate. Despite the CSM density of SN 2021efd not corresponding perfectly to the steady mass loss model, an order of magnitude for the mass-loss rate can be seen to be near $\sim 10^{-3} - 10^{-2}$ $M_\odot$ yr^{-1} with 10^{-3} $M_\odot$ yr^{-1} acting as a lower limit. The CSM velocity is directly proportional to the mass-loss rate, as can be seen from eq 3. A comparison of the interaction powered luminosity to calculations with other CSM velocities is displayed in Appendix C. The luminosity is directly proportional to the efficiency ϵ. This is the biggest uncertainty in the estimate. However, we can see from figure 18 that even a change by a factor of two $\epsilon = 0.05 - 0.2$, does not change the order of magnitude estimate. This is equivalent to adding or subtracting luminosity by $\log_{10}(2) = 0.3$.

Figure 19 displays the accreted mass over time. From this figure, it can be seen that the lower limit of the CSM mass is 10^{-1} $M_\odot$. This is a lower limit since the interaction continues to later epochs. From light curves in figure 5, we can see there is excess flux till at least $\sim$ 400 days.

7 Discussion

I have presented observations of SN 2021efd, which is a Type Ib SN with a peculiar light curve. There is excess energy in the light curve compared to what is caused by the nickel decay. Bumpy light curves have been associated with interaction previously, e.g. in SN 2019tsf [29][30]. Lorentzian wings in the line profiles in nebular spectra have also been connected to the scattering of photons by free electrons in ionized CSM (eg. [32][33]). Excessive flux in the iron complex in nebular spectra is also found in other interacting SNe (e.g.[34],[35]). With all these signs and the lack

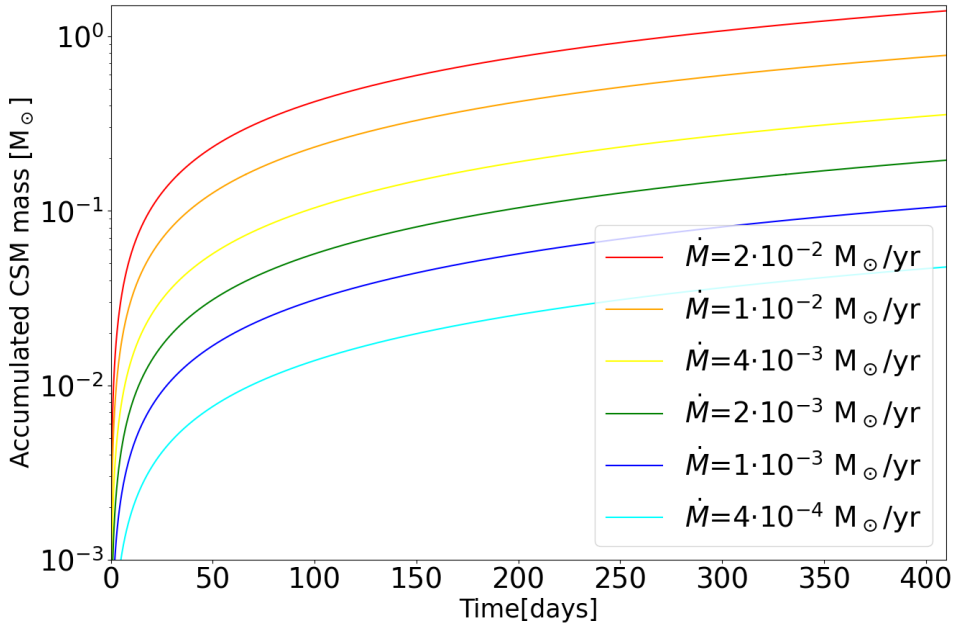

Figure 19. The mass of the shock shell has accumulated from the CSM at each epoch according to the values used in the calculated interaction luminosity. Effectively this tells us the CSM mass up to a certain range from the SN.

of hydrogen features in the early and nebular spectra, I conclude that SN 2021efd is interacting with H-poor CSM. The absence of narrow helium lines can be explained by the high binding energy of the helium atom. The ionization degree of helium in the CSM can remain low and so can the excitation rate.

The helium shell stripping is a phase all progenitors of Type Ic SNe undergo. This means the mass loss happens long before the explosion of the SN and the lost shell has had time to travel beyond where the ejecta reaches while the SN is luminous. The progenitor of SN 2021efd might be a star that was in the process of shedding its He-layer when it exploded.

By assuming the CSM to be in a spherical shell and the mass loss to be steady, I derive a mass-loss rate of $\sim 10^{-3} - 10^{-2}$ M$_\odot$ yr^{-1}. A spherical CSM distribution is not expected from all mass-loss mechanisms. The comparison of the interaction luminosity of SN 2021efd to the calculated interaction luminosity, suggests that

the mass-loss rate might have decreased over time. The bumpiness of the light curve suggests a clumpy CSM distribution. Whether the mass was initially lost in eruptions or steadily and formed clumps later, e.g. due to changes in the velocity of the ejected material, requires further investigation. If this mass-loss mechanism does not change with time and is the same mechanism that is responsible for helium layer stripping in progenitors of Type Ic SNe, then the helium envelope of a few solar masses would be stripped in $\sim 10^{-2} - 10^{-3}$ yr.

Since the CSM is H-poor it likely did not originate from the companion star. The primary star begins helium core burning earlier and loses its hydrogen layer earlier. The companion star accretes a fraction of this hydrogen. The progenitor of SN 2021efd must be the primary star since the resulting SN has no hydrogen features in its spectra. If the companion star lost its hydrogen layer after the primary star, the primary star would gain a fraction of the lost hydrogen. The companion star is hydrogen-rich and can not have lost its helium layer either. The likelihood that the CSM originated from the companion star is low even if some other mass-loss mechanism was responsible. It would require a companion star to be losing large amounts of H-poor material right at the time of the explosion of the progenitor and such a mass loss event can not be happening for much longer than the value derived above. Thus we can conclude the CSM to have likely originated from the progenitor of SN 2021efd.

Line-driven wind mass-loss rate is much lower ($\sim 10^{-5}$ $M_\odot$ yr^{-1}) than the derived mass-loss rate [8]. With small enough binary separation and high enough metallicity binary interaction could cause mass loss even in the helium layer. Binary interaction does not explain the bumpy structure of the light curve. The CSM must be either clumpy or the mass-loss rate must have increased and decreased multiple times.

It remains possible that the mass was lost in eruptions possibly during the later burning phases of the stellar core. The time scale for the mass loss of $\sim 10^{-2} - 10^{-3}$

yr is similar to the carbon-burning phase in the stellar core.

The progenitor mass of SN 2021efd is estimated with the [O I]/[Ca II] and compared to helium star masses in simulated SESNe. A progenitor star ZAMS mass of $\sim$ 25 M $_{\odot}$ is estimated. Type Ic SNe progenitors are typically expected to have greater ZAMS masses than Type Ib SNe progenitors. Depending on metallicity, a ZAMS mass of $\sim$ 25 M $_{\odot}$ is compatible with progenitors of both Type Ib SNe and Type Ic SNe [49][50]. However, a few things need to be noted from this mass estimate. SN 2021efd is interacting with CSM, which is likely He-rich and originates from its progenitor star. At the time of the explosion, the helium star had already thinned and lost substantial mass (see figure 19). On the other hand, the [O I]/[Ca II] ratio as a progenitor star estimate has large uncertainties. In the models of [41] the [O I]/[Ca II] ratio does not rise monotonically with helium star mass and evolves with time. The flux measurement is also obscured by the nearby [N II] and [Fe II] lines.

The [O I]/[Ca II] ratio itself can be compared to typical values of SESNe. It has been found that Type IIb and Type Ib have similar [O I]/[Ca II] flux ratios but Type Ic have typically higher values although overlapping with IIb/Ib [51]. Comparing to typical values reported in figure 3. of [40]. SN 2021efd sits in the overlapping region of SESNe. The [O I]/[Ca II] ratio of SN 2021efd therefore does not separate it clearly from typical Type Ib SNe. The effect of interaction on the [O I]/[Ca II] ratio is unknown.

The ejecta velocity of SN 2021efd inferred from both He I and Fe II lines of the spectra early epochs is in the range of what is typical for SESNe figure 15. Where the He I velocity is around the higher end for a SESN, the Fe II velocity is at the lower end. Line formation depends on many factors

The ejecta mass and kinetic energy of the ejecta can be compared to literature values. When compared to values inferred for the sample of SESNe studied in [27]

both values are found to be within range of both Type Ib SNe and Type Ic SNe. If some of the parameters measured here were consistent with Type Ic SNe but not with regular Type Ib SNe or vice versa, it would hint toward the cause of the helium layer stripping. However, all parameters obtained in this thesis except the mass-loss rate are within the range of Type Ib SNe.

8 Conclusion

In this thesis, I have studied the unique SN 2021efd. I suggested that SN 2021efd might contain clues to the mass-loss mechanism of stars that have lost their He-layer. To this end I have confirmed the original classification as Type Ib SN and that SN 2021efd is interacting with H-poor CSM.

I derived a mass-loss rate of $\sim 10^{-3} - 10^{-2}$ $M_\odot$ yr^{-1} by assuming a steady mass-loss rate, a wind velocity of 100 km s^{-1}, an efficiency ϵ value of 0.1, and a spherical CSM distribution. This corresponds to a mass-loss period duration of $\sim 10^{-2} - 10^{-3}$ yr for the helium layer of a few solar masses.

I derived the parameters of the SN and progenitor star. For kinetic energy and ejecta mass, I derived $\sim 1.2 \cdot 10^{51}$ ergs and ~ 2.2 $M_\odot$. These parameters are within the overlapping range of Type Ib and Ic SNe.

The progenitor star ZAMS mass is ~ 25 $M_\odot$ from the [O I]/[Ca II] ratio. The value for the [O I]/[Ca II] ratio is ~ 1.3. This value compared to values from the literature lies in the overlapping region of Type Ib and Ic SNe, i.e., the ratio is not particularly high.

9 Acknowledgments

I would like to thank my supervisors Hanindyo Kuncarayakti and Takashi Nagao for their invaluable guidance in the creation of this thesis. I also give thanks to Seppo

Mattila, Tuomas Kangas, and the UTU transient group. I am grateful to my family for all the support throughout my education.

This work has made use of data from the Asteroid Terrestrial-impact Last Alert System (ATLAS) project. The Asteroid Terrestrial-impact Last Alert System (ATLAS) project is primarily funded to search for near earth asteroids through NASA grants NN12AR55G, 80NSSC18K0284, and 80NSSC18K1575; byproducts of the NEO search include images and catalogs from the survey area. This work was partially funded by Kepler/K2 grant J1944/80NSSC19K0112 and HST GO-15889, and STFC grants ST/T000198/1 and ST/S006109/1. The ATLAS science products have been made possible through the contributions of the University of Hawaii Institute for Astronomy, the Queen's University Belfast, the Space Telescope Science Institute, the South African Astronomical Observatory, and The Millennium Institute of Astrophysics (MAS), Chile.

Based on observations obtained with the Samuel Oschin Telescope 48-inch and the 60-inch Telescope at the Palomar Observatory as part of the Zwicky Transient Facility project. ZTF is supported by the National Science Foundation under Grant No. AST-2034437 and a collaboration including Caltech, IPAC, the Weizmann Institute for Science, the Oskar Klein Center at Stockholm University, the University of Maryland, Deutsches Elektronen-Synchrotron and Humboldt University, the TANGO Consortium of Taiwan, the University of Wisconsin at Milwaukee, Trinity College Dublin, Lawrence Livermore National Laboratories, and IN2P3, France. Operations are conducted by COO, IPAC, and UW.

This research has made use of the Spanish Virtual Observatory (https://svo.cab.inta-csic.es) project funded by MCIN/AEI/10.13039/501100011033/ through grant PID2020-112949GB-I00

References

[1] A. Gal-Yam. "Observational and Physical Classification of Supernovae". In: *Handbook of Supernovae*. Ed. by A. W. Alsabti and P. Murdin. 2017, p. 195.

[2] T. Kangas et al. "The Zwicky Transient Facility phase I sample of hydrogen-rich superluminous supernovae without strong narrow emission lines". In: *Monthly Notices of the Royal Astronomical Society* 516.1 (Oct. 2022), pp. 1193–1218.

[3] A. Gal-Yam. "The Most Luminous Supernovae". In: *Annual Review of Astronomy & Astrophysics* 57 (Aug. 2019), pp. 305–333.

[4] D. Branch and J. C. Wheeler. *Supernova Explosions*. 2017.

[5] T. Nagao. "Circumstellar environments of Supernovae, PhD Thesis". In: (Jan. 2019).

[6] A. Gilkis and I. Arcavi. "How much hydrogen is in Type Ib and IIb supernova progenitors?" In: *Monthly Notices of the Royal Astronomical Society* 511.1 (Mar. 2022), pp. 691–712.

[7] S. Hachinger et al. "How much H and He is 'hidden' in SNe Ib/c? - I. Low-mass objects". In: *Monthly Notices of the Royal Astronomical Society* 422.1 (May 2012), pp. 70–88.

[8] R. A. Chevalier and C. Fransson. "Thermal and Non-thermal Emission from Circumstellar Interaction". In: *Handbook of Supernovae*. Ed. by A. W. Alsabti and P. Murdin. 2017, p. 875.

[9] J. D. Lyman et al. "Bolometric light curves and explosion parameters of 38 stripped-envelope core-collapse supernovae". In: *Monthly Notices of the Royal Astronomical Society* 457.1 (Mar. 2016), pp. 328–350.

[10] T. Kangas et al. "Core-collapse supernova progenitor constraints using the spatial distributions of massive stars in local galaxies". In: *Astronomy & Astrophysics* 597, A92 (Jan. 2017), A92.

[11] J. J. Eldridge and J. S. Vink. "Implications of the metallicity dependence of Wolf-Rayet winds". In: *Astronomy & Astrophysics* 452.1 (June 2006), pp. 295–301.

[12] S.-C. Yoon, L. Dessart, and A. Clocchiatti. "Type Ib and IIb Supernova Progenitors in Interacting Binary Systems". In: *The Astrophysical Journal* 840.1, 10 (May 2017), p. 10.

[13] C. Pellegrino et al. "The Diverse Properties of Type Icn Supernovae Point to Multiple Progenitor Channels". In: *The Astrophysical Journal* 938.1, 73 (Oct. 2022), p. 73.

[14] F. J. Masci et al. "The Zwicky Transient Facility: Data Processing, Products, and Archive". In: *Publications of the Astronomical Society of the Pacific* 131.995 (Jan. 2019), p. 018003.

[15] Sloan Digital Sky Survey. "Sloan Digital Sky Survey Data Release 13 as obtained". In: 2016SDSSD.C...0000: (Jan. 2017).

[16] A. Reguitti and M. Stritzinger. "POISE Transient Classification Report for 2021-03-04". In: *Transient Name Server Classification Report* 2021-682 (Mar. 2021), pp. 1–682.

[17] J. L. Tonry et al. "ATLAS: A High-cadence All-sky Survey System". In: *Publications of the Astronomical Society of the Pacific* 130.988 (June 2018), p. 064505.

[18] K. W. Smith et al. "Design and Operation of the ATLAS Transient Science Server". In: *Publications of the Astronomical Society of the Pacific* 132.1014, 085002 (Aug. 2020), p. 085002.

[19] D. J. Schlegel, D. P. Finkbeiner, and M. Davis. "Maps of Dust Infrared Emission for Use in Estimation of Reddening and Cosmic Microwave Background Radiation Foregrounds". In: *The Astrophysical Journal* 500.2 (June 1998), pp. 525–553.

[20] R. Indebetouw et al. "The Wavelength Dependence of Interstellar Extinction from 1.25 to 8.0 μm Using GLIMPSE Data". In: *The Astrophysical Journal* 619.2 (Feb. 2005), pp. 931–938.

[21] C. Rodrigo, E. Solano, and A. Bayo. *SVO Filter Profile Service Version 1.0*. IVOA Working Draft 15 October 2012. Oct. 2012.

[22] C. Rodrigo and E. Solano. "The SVO Filter Profile Service". In: *XIV.0 Scientific Meeting (virtual) of the Spanish Astronomical Society*. July 2020, 182, p. 182.

[23] S. Jester et al. "The Sloan Digital Sky Survey View of the Palomar-Green Bright Quasar Survey". In: *AJ* 130.3 (Sept. 2005), pp. 873–895.

[24] S. Srivastav, G. C. Anupama, and D. K. Sahu. "Optical observations of the fast declining Type Ib supernova iPTF13bvn". In: *Monthly Notices of the Royal Astronomical Society* 445.2 (Dec. 2014), pp. 1932–1941.

[25] M. W. Richmond et al. "UBVRI Photometry of SN 1993J in M81: The First 120 Days". In: *Astronomical Journal* 107 (Mar. 1994), p. 1022.

[26] D. J. Hunter et al. "Extensive optical and near-infrared observations of the nearby, narrow-lined type Ic <ASTROBJ>SN 2007gr</ASTROBJ>: days 5 to 415". In: *Astronomy & Astrophysics* 508.1 (Dec. 2009), pp. 371–389.

[27] F. Taddia et al. "The Carnegie Supernova Project I. Analysis of stripped-envelope supernova light curves". In: *Astronomy & Astrophysics* 609, A136 (Feb. 2018), A136.

[28] G. Hosseinzadeh et al. "Type Ibn Supernovae Show Photometric Homogeneity and Spectral Diversity at Maximum Light". In: *The Astrophysical Journal* 836.2, 158 (Feb. 2017), p. 158.

[29] J. Sollerman et al. "Two stripped envelope supernovae with circumstellar interaction. But only one really shows it". In: *Astronomy & Astrophysics* 643, A79 (Nov. 2020), A79.

[30] Y. Zenati et al. "Evidence for Extended Hydrogen-Poor CSM in the Three-Peaked Light Curve of Stripped Envelope Ib Supernova". In: *ArXiv e-prints*, arXiv:2207.07146 (July 2022), arXiv:2207.07146.

[31] M. D. Stritzinger et al. "The Carnegie Supernova Project I. Methods to estimate host-galaxy reddening of stripped-envelope supernovae". In: *Astronomy & Astrophysics* 609, A135 (Feb. 2018), A135.

[32] H. Kuncarayakti et al. "The broad-lined Type-Ic supernova SN 2022xxf and its extraordinary two-humped light curves. I. Signatures of H/He-free interaction in the first four months". In: *Astronomy & Astrophysics* 678, A209 (Oct. 2023), A209.

[33] J. Sollerman et al. "Two stripped envelope supernovae with circumstellar interaction. But only one really shows it". In: *Astronomy & Astrophysics* 643, A79 (Nov. 2020), A79.

[34] H. Kuncarayakti et al. "Late-time H/He-poor Circumstellar Interaction in the Type Ic Supernova SN 2021ocs: An Exposed Oxygen-Magnesium Layer and Extreme Stripping of the Progenitor". In: *The Astrophysical Journal Letters* 941.2, L32 (Dec. 2022), p. L32.

[35] L. Tartaglia et al. "SN 2018ijp: the explosion of a stripped-envelope star within a dense H-rich shell?" In: *Astronomy & Astrophysics* 650, A174 (June 2021), A174.

[36] S. Holmbo et al. "The Carnegie Supernova Project I. Spectroscopic analysis of stripped-envelope supernovae". In: *Astronomy & Astrophysics* 675, A83 (July 2023), A83.

[37] W. D. Arnett. "Type I supernovae. I - Analytic solutions for the early part of the light curve". In: *The Astrophysical Journal* 253 (Feb. 1982), pp. 785–797.

[38] D. Arnett. *Supernovae and Nucleosynthesis: An Investigation of the History of Matter from the Big Bang to the Present*. 1996.

[39] E. Chatzopoulos et al. "Analytical Light Curve Models of Superluminous Supernovae: χ^2-minimization of Parameter Fits". In: *The Astrophysical Journal* 773.1, 76 (Aug. 2013), p. 76.

[40] Q. Fang et al. "A hybrid envelope-stripping mechanism for massive stars from supernova nebular spectroscopy". In: *Nature Astronomy* 3 (Mar. 2019), pp. 434–439.

[41] L. Dessart et al. "Modeling of the nebular-phase spectral evolution of stripped-envelope supernovae. New grids from 100 to 450 days". In: *Astronomy & Astrophysics* 677, A7 (Sept. 2023), A7.

[42] S. E. Woosley. "The Evolution of Massive Helium Stars, Including Mass Loss". In: *The Astrophysical Journal* 878.1, 49 (June 2019), p. 49.

[43] T. Ertl et al. "The Explosion of Helium Stars Evolved with Mass Loss". In: *The Astrophysical Journal* 890.1, 51 (Feb. 2020), p. 51.

[44] R. A. Chevalier and C. Fransson. "Supernova Interaction with a Circumstellar Medium". In: *Supernovae and Gamma-Ray Bursters*. Ed. by K. Weiler. Vol. 598. 2003, pp. 171–194.

[45] T. J. Moriya et al. "An analytic bolometric light curve model of interaction-powered supernovae and its application to Type IIn supernovae". In: *Monthly Notices of the Royal Astronomical Society* 435.2 (Oct. 2013), pp. 1520–1535.

[46] K. F. Riley, M. P. Hobson, and S. J. Bence. *Mathematical Methods for Physics and Engineering Third Edition Paperback Set*. 2006.

[47] C. Leitherer. "Mass Loss from LBVs: Observational Constraints". In: *Luminous Blue Variables: Massive Stars in Transition*. Ed. by A. Nota and H. Lamers. Vol. 120. Astronomical Society of the Pacific Conference Series. Jan. 1997, p. 58.

[48] T. J. Moriya et al. "Light-curve modelling of superluminous supernova 2006gy: collision between supernova ejecta and a dense circumstellar medium". In: *Monthly Notices of the Royal Astronomical Society* 428.2 (Jan. 2013), pp. 1020–1035.

[49] C. Georgy et al. "The different progenitors of type Ib, Ic SNe, and of GRB". In: *Astronomy & Astrophysics* 502.2 (Aug. 2009), pp. 611–622.

[50] H. Kuncarayakti et al. "Constraints on core-collapse supernova progenitors from explosion site integral field spectroscopy". In: *Astronomy & Astrophysics* 613, A35 (May 2018), A35.

[51] Q. Fang et al. "Statistical Properties of the Nebular Spectra of 103 Stripped-envelope Core-collapse Supernovae". In: *The Astrophysical Journal* 928.2, 151 (Apr. 2022), p. 151.

Appendix A: Bolometric light curve all epochs

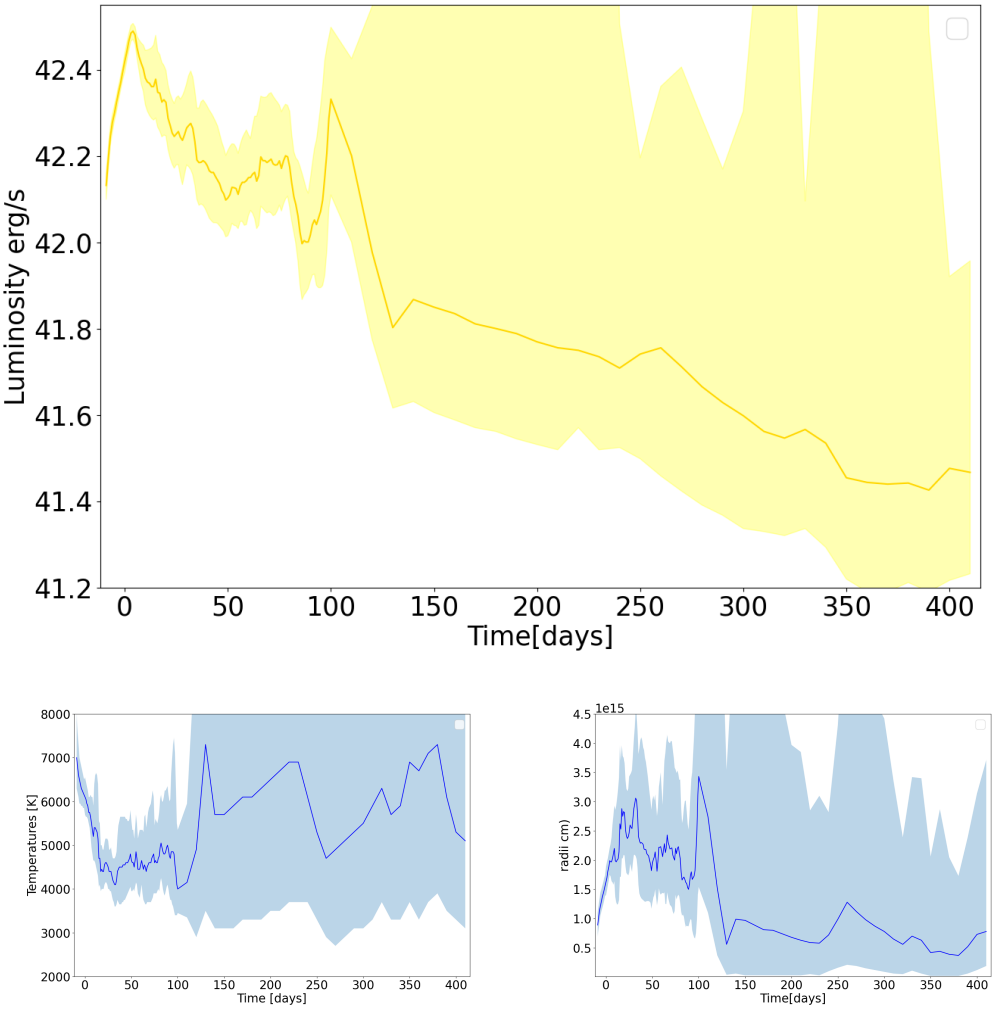

Figure 20. Results of the SED fitting. Top: the bolometric light curve of SN 2021efd. Center: Temperature of the photosphere. Bottom: Radius of the photosphere. The plots here are over all epochs with photometric data. Errors are the 1-σ limits of the fit. The errors from $\sim$ 120 days onward reach the upper and lower values iterated through ($1500 - 200000$ K and $10^{13} - 15 \cdot 10^{15}$ cm), which reach unphysical values. Effectively the 1-σ limit does not converge.

Appendix B: Numerical Runge-Kutta method

The Runge-Kutta method is a numerical method for solving differential equations. I explain the Runge-Kutta method and how I adapted it to solve the EOM. In the equations below, subscripts c and n stand for current and next. This is because the code is iterated through many times. The values $r_{c/n}$ and $v_{c/n}$ refer to the shock shell. The values are updated for the next loop in every iteration. The time step between iterations is $t_n = t_c + \Delta t$.

$$
\begin{aligned}
k_1 &= \Delta t\ v_c \\
l_1 &= \Delta t\ F(r_c, v_c, t_c)/M_{\rm sh} \\
k_2 &= \Delta t\ (v_c + l_1/2) \\
l_2 &= \Delta t\ F(r_c + k_1/2, v_c + l_1/2, t_c + \Delta t/2)/M_{\rm sh} \\
k_3 &= \Delta t\ (v_c + l_2/2) \\
l_3 &= \Delta t\ F(r_c + k_2/2, v_c + l_2/2, t_c + \Delta t/2)/M_{\rm sh} \\
k_4 &= \Delta t\ (v_c + l_3) \\
l_4 &= \Delta t\ F(r_c + k_3, v_c + l_3, t_c + \Delta t)/M_{\rm sh} \\
v_n &= v_c + (l_1 + 2l_2 + 2l_3 + l_4)/6 \\
r_n &= r_c + (k_1 + 2k_2 + 2k_3 + k_4)/6
\end{aligned}
$$

$F(r_{\rm sh}, v_{\rm sh}, t)/M_{\rm sh}$ is the acceleration of the shock shell. The mass of the shock shell is $M_{\rm sh}$. F is the force directed at the shock shell:

$$F(r_{\rm sh}, v_{\rm sh}, t) = 4\pi r_{\rm sh}^2(\rho_{ej}(r_{\rm sh}, t)(v_{ej} - v_{\rm sh})^2 - \rho_{csm}(r_{\rm sh})(v_{\rm sh} - v_w)^2)$$

The Runge-Kutta method works not just by adding $v_{\rm sh}\Delta t$ to $r_{\rm sh}$ and $\dfrac{F}{M_{\rm sh}}\Delta t$ to $v_{\rm sh}$ in small time steps but by also approximating the change of the slope between the time steps. The k and l values describe the slope of $r_{\rm sh}$ and $v_{\rm sh}$ between the iterations. As can be seen from the bottom two equations, what is eventually added to $r_{\rm sh}$ and $v_{\rm sh}$ is *effectively* the weighted average of many approximations of the slopes multiplied by the time step.

Appendix C: Interaction model with different CSM velocities

The calculated interaction luminosities in figure 18 used the value of 100 km s^{-1}. This is an assumption. Due to the unknown nature of the mass-loss mechanism, the velocity may differ drastically. Figure 21 displays the comparison of the interaction luminosity of SN 2021efd to calculated interaction luminosities with different CSM velocities and single mass-loss rate of $\sim 10^{-3}$ $M_\odot$ yr^{-1}. The increase of the velocity needs a higher mass-loss rate to match the observed luminosity as the density of the CSM decreases with CSM velocity.

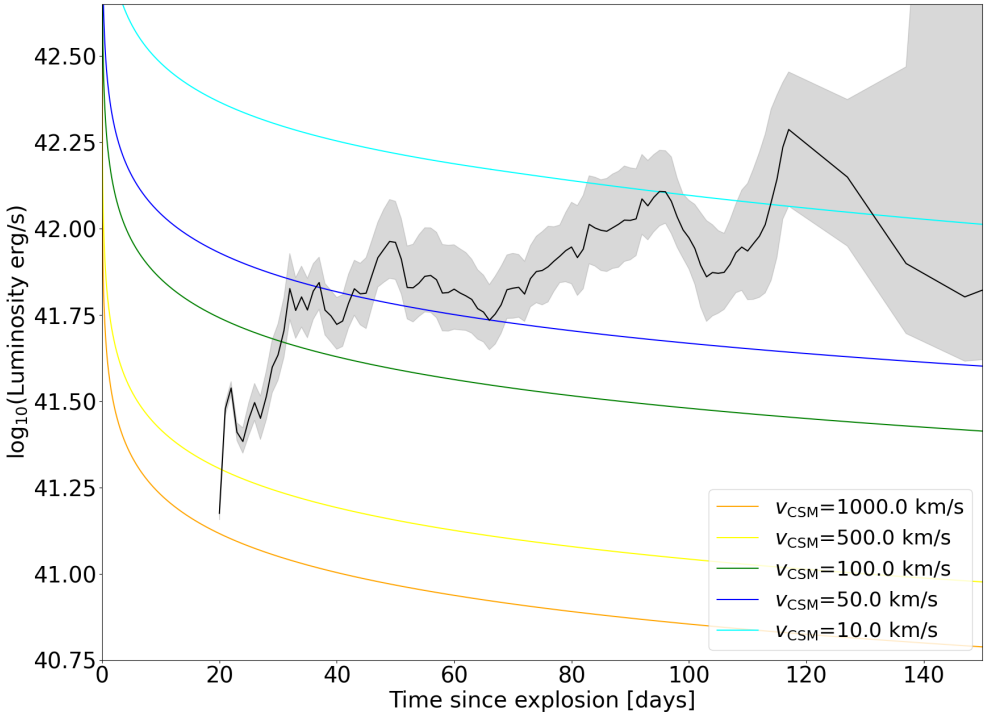

Figure 21. SN component reduced light curve of SN 2021efd compared with calculated interaction luminosities with different CSM velocities and 10^{-3} $M_\odot$ yr^{-1}.